The Prediction of Turbulent Boundary Layer Noise

Steven A. E. Miller*

Turbulent boundary layers, which are observed in almost all aerospace vehicles and in natural phenomena, radiate acoustic waves. A closed-form mathematical model is proposed to predict the intensity and coherence of acoustic radiation from turbulent boundary layers. For this purpose the Navier-Stokes equations are rearranged and solved using a cross-spectral acoustic analogy. Arguments of the model are the spatial two-point cross-correlations of the turbulent statistics and mean flow of the turbulent boundary layer. These arguments are modeled using relations whose coefficients are calibrated with numerical and measurement data drawn from a wide range of sources. Models for turbulent statistics are proposed for the zero pressure gradient turbulent boundary layer at a wide range of ambient Mach numbers. Predictions of acoustic intensity, spatial coherence, and model arguments are validated with numerical and measurement data. Predicted sound pressure levels agree well with numerical results. The variation of the near-field, mid-field, and far-field decay of acoustic intensity is investigated. The decay of spatial coherence is demonstrated to be a reflection of the turbulent statistics within the boundary layer. Finally, analysis of the model equation shows that it is consistent with canonical theory.

Nomenclature

Symbols	Description
c	Speed of sound
c_f	Skin friction
c_i	Constants
F_{ijlm}	Far-field term
f	Frequency
G	Cross-power spectral density
$\mathcal{I}_\tau$	Integrated terms with respect to τ^{th} derivative
k	Turbulent kinetic energy
l_{si}	Turbulent length scale in direction i
M_{ijlm}	Mid-field term
N_{ijlm}	Near-field term
$\boldsymbol{R}_{ijlm}$	Model of two-point cross-correlation of Lighthill stress tensor
R	Normalized two-point cross-correlation
R_c	Recovery factor
$\boldsymbol{r}$	Vector from source to observer
S	Auto-power spectral density
t	Observer time
T_{ij}	Lighthill stress tensor
T	Temperature
$\boldsymbol{u}$	Fluid velocity
$\boldsymbol{x}$	Observer position
u_τ	Wall friction velocity
V	Volume that boundary layer encompasses
x_l	Streamwise location of velocity profile from leading edge
u^+	Velocity coordinate (uu_τ^{-1})
$\boldsymbol{y}$	Source position
y^+	Wall coordinate ($u_\tau y \nu^{-1}$)

Greek Symbols

Δ_1	Parameter of integration
δ	Boundary layer thickness
δ_{ij}	Kronecker delta function
$\boldsymbol{\eta}$	Vector between sources
η	Cross-stream source separation
θ	Momentum thickness
Π	Coles wake factor
ξ	Streamwise source separation
κ	Von Karman constant
ρ	Density
ρ_w	Density at wall
τ	Retarded time
τ_s	Turbulent time scale
τ_w	Wall shear stress
ν	Kinematic viscosity
ζ	Spanwise source separation
ω	Radial frequency

Non-Dimensional Numbers

$\mathcal{M}$	Vector Mach number
$\mathcal{R}e$	Reynolds number
$\mathcal{R}e_{K_p}$	Porous Reynolds number
$\mathcal{S}t$	Strouhal number

Abbreviations

BBSAN	Broadband shock-associated noise
CPSD	Cross-power spectral density
CSAA	Cross-spectral acoustic analogy
DNS	Direct numerical simulation
LES	Large eddy simulation
PIV	Particle image velocimetry
SPL	Sound pressure level

*Assistant Professor, The Department of Mechanical and Aerospace Engineering, The University of Florida, 231 MAE-A, P.O. Box 116250, Gainesville, FL, 32611, USA, AIAA Senior Member, saem@ufl.edu

Introduction

Prandtl's[1] 1904 lecture, 'On Fluid Motion with Very Small Friction,' laid the framework of boundary layer theory by using a theoretical approach guided by experiments that revolutionized the field of fluid dynamics. Kovasznay[2] writes that the boundary layer, '*exhibits the details one normally associates with confined flows, termed "wall turbulence." In these respects it is similar to channel and pipe flow. On the other hand, near to the free boundary it incorporates the features of "free turbulence" found in wakes and jets.*' The flow exhibits self-similarity and is driven by instabilities that lead to turbulence, and the turbulence decays through an energy cascade that is dissipated into internal energy and acoustic radiation. Kline et al.[3] summarize this process, '*production of turbulence near the wall in such a flow arises primarily from a local, short-duration, intermittent dynamic instability of the instantaneous velocity profile... This instability acts not to alter the mean field flow but rather to maintain it. The ejection of fluid away from the wall in the subsequent process is felt to be the central mechanism for energy, momentum, and vorticity transfer between the inner and outer layers.*' The instabilities and large-scale turbulence exhibit significant coherence within the boundary layer, and this coherence is observed within the acoustically radiated field. Figure 1 shows a photograph created by Lee et al.[4] of a turbulent boundary layer. A dye is injected into the flow upstream of a moving flat plate within a water channel and is illuminated by laser induced fluorescence. One can observe the turbulence in the boundary layer and many large coherent structures. For reviews of boundary layer turbulence examine Kovasznay,[2] Kline et al.,[3] or Eichelbrenner,[5] and for a comprehensive introduction examine Schlichting.[6] In this paper, we predict the acoustic radiation and its coherence from a turbulent boundary layer.

Early two-point measurements within the turbulent boundary layer confirmed theories regarding the existence of coherent structures. Coherent motion is defined as having significant correlation of one or more field-variables over a spatial range that is larger than that exhibited by the small-scale structures. In early efforts to characterize coherent structures, numerous measurements of two-point statistics using hot-wires were conducted by varying their streamwise and cross-stream positions. For example, Hunt et al.[7] showed two-point correlations have self-similarity in the cross-stream direction, even within the near-wall region that is statistically inhomogeneous. Not long after, Hunt et al.[8] showed that cross-correlation derived length scales are related to the length scales that can be derived from the local turbulent kinetic energy and dissipation rate. One contemporary approach for finding two-point correlations is particle image velocimetry (PIV), which is non-intrusive except for the requirement of flow seeding. For example, Naka et al.[9] calculated space-time pressure-velocity correlations within a turbulent boundary layer using stereoscopic PIV and surface pressure transducers, where strong empirical evidence showed that the wall pressure fluctuations are highly coherent with large-scale structures of turbulence. Turbulent boundary layers often exhibit self-similar large-scale coherent structures. Readers should consult Robinson[10] for a review regarding large-scale coherent structures of turbulent boundary layers, which play an important role in this work.

The effects of compressibility on boundary layer turbulence are difficult to ascertain because most studies are restricted to low Reynolds numbers due to limited facility or computational resources. Robinson[11] examined compressibility effects using dual hot-wire probes at $\mathcal{M}_\infty = 2.97$, and showed that compressible and incompressible flows are similar except for some additional intermittency that only occurs within a narrow region. Spina and Smits[12] examined a $\mathcal{M}_\infty = 2.87$ boundary layer and used conditional sampling to study the structure, angle, and intermittency of coherent structures, and similarity was shown for compressible flows. Robinson's[11] experiment provided strong evidence that the Morkovin[13] hypothesis, that the essential dynamics of compressible boundary layers are similar to incompressible boundary layers, is correct.

As shown theoretically by Powell[14] and confirmed by Naka et al.,[9] pressure fluctuations on the wall, among other quantities, are due to turbulence. Spatial coherence of wall quantities is an 'imprint' of the large-scale coherent structures within the turbulent boundary layer. For example, Rackl and Weston[15] examined fluctuations on a Tupolev 144LL aircraft and showed that the empirical model of Efimtsov[16] for length scale based on wall pressure agreed well with experiment. Palumbo[17] examined the correlation and coherence lengths of wall fluctuations based on data from the Gulfstream G550 aircraft operating at flight Mach numbers of 0.56, 0.70, and 0.86. In this case, however, an Efimtsov[16] model with modified coefficients fit measurement data. These measurements are extremely important, as they are highly correlated with the large-scale turbulent structures within the boundary layer, which are the source of aerodynamic noise. The shape or structure of the wall has an effect on the turbulence that in turn changes the resultant response of the wall pressure spectrum. Increased surface roughness and its effect on the flow was examined by Alexander et al.[18] The effect of a porous wall was examined by Manes et al.,[19] and they showed how the von Karman coefficient changes the velocity profile as a function of porous Reynolds number.

A limited number of experiments directly measured radiated noise from turbulent boundary layers. A very notable effort was made by Greshilov and Mironov,[20] who used a hydrophone to measure the sound generated in a low speed water channel with velocities between 3.7 and 12 ms^{-1}. They attempted to relate the wavenumber spectrum of tangential forces on the duct wall to acoustic intensity. Duell et al.[21] examined boundary layer noise within aeroacoustic wind tunnels that had both closed-wall and open jet test sections. Boundary layer noise is shown to greatly contribute to the overall background noise of the tunnel, especially at frequencies lower than 500 Hz. Like Alexander et al.[18] who examined surface roughness, Smith et al.[22] measured the variation of noise with the addition of surface elements to simulate varying roughness.

Perhaps the first model for the prediction of noise from a turbulent boundary layer was developed by Powell.[14] Powell[14] employed Lighthill's acoustic analogy in conjunction with a mirror source (that effectively models reflection of sound waves from the wall) and found an expression for the acoustic power. He showed acoustic power is proportional to the volumetric integral of the second time derivative of the Lighthill stress tensor multiplied by $\rho_\infty^{-1} c_\infty^{-5}$. Analysis of Powell[14] shows that pressures on the wall are only the aerodynamic 'imprint' of turbulence, and the recent work of Naka et al.[9] supports this viewpoint. The perceived so-called dipoles are only due to the presence of quadrupoles. Powell[14] showed no predictions relative to measurement.

In a series of papers, Ffowcs Williams[23,24] and Ffowcs Williams and Purshouse[25] examined the noise due to turbulent boundary layers. Ffowcs Williams[23] wrote, '*The radiation remains quadrupole in character. The surface merely accounts for a reflection of the turbulence-generated sound, with the reflection coefficient being identical to that of plane acoustic waves.*' Ffowcs Williams[24] examined the effect of porous liners in place of a hard wall and showed additional noise is scattered with wavenumbers that are close to the orifice sizes. A final philosophical paper of Ffowcs Williams and Purshouse[25] models the boundary layer as a vortex sheet of constant cross-stream velocity and models the pressure with the Poisson equation. No predictions are shown within these papers, thus it is difficult to justify the validity of their theories.

As the pressure on the wall is an imprint of the large-scale turbulence within the boundary layer, it is tempting to create a prediction model for the acoustic radiation that is dependent on the wall wavenumber pressure spectrum. One such empirical approach by Howe[26] related the wall wavenumber pressure spectrum to the acoustic spectrum. The benefit of this approach is that existing readily available empirical models of the wall wavenumber pressure spectrum are the main argument of the model. Similar to the model of Howe,[26] Glegg et al.[27] created a model that depends on the wavenumber spectrum of the surface pressure fluctuations, and additionally included a correlation function for the surface roughness distribution. Unfortunately, the paper showed no comparison with measurement.

The rapid advancement of digital computers has allowed for numerical solutions of the governing equations. Hu et al.[28,29] performed a direct numerical simulation (DNS) combined with an acoustic analogy and a half-space Green's function. They argued that noise from an equivalent dipole source was dominant at Mach numbers greater than 0.1. Their finding conflicts with the work of Powell,[14] Naka et al.,[9] and Ffowcs Williams,[23] and the recent large-eddy simulation (LES) simulation of Gloerfelt and Berland.[30]

Recently Gloerfelt and Berland[30] and Gloerfelt and Margnat[31] performed an LES of a compressible turbulent boundary layer at three high speed Mach numbers. They confirmed that the acoustic radiation is due to the turbulence and not from its imprint on the wall. They predicted the acoustic radiation at observers directly contained within the computational domain and also with a Ffowcs Williams-Hawkings solver, which showed excellent agreement. Their predictions of boundary layer mean flow and turbulent statistics agreed very well with other numerical simulations and measurements. Predictions of the root mean square velocities compared well with other turbulence models. These excellent numerical simulations (some might call a 'numerical experiment') are the basis for the validation of the model presented in this paper.

Recently Miller[32] developed the cross-spectral acoustic analogy (CSAA), which is capable of predicting the near-field cross-spectra of acoustic pressure from an arbitrary turbulent field in motion. When both observers are placed at the same spatial location the model predicts the auto-spectra of acoustic pressure. If the observers are at the same location and in the far-field, then the model reduces to the Lighthill acoustic analogy in the frequency domain. The model was used to predict the near-field and far-field, auto-spectrum and coherence, of acoustic pressure from a wide range of turbulent jets. Recently the CSAA was successfully applied to the prediction of broadband shock-associated noise (BBSAN) by Miller.[33] The CSAA is the basis of this paper, and it requires knowledge of the statistics within the turbulent field, which is the turbulent boundary layer.

Acoustic analogies that are based on the wave equation, such as those of Lighthill[34,35] and the one used in this paper, do not directly account for the effect of refraction of sound propagation by the meanflow. Hanson

and Magliozzi,[36] Mcaninch and Rawls,[37] and Lu[38] examined the effects of sound propagation, refraction, and resultant scattering of acoustic waves within boundary layers on aircraft fuselage. These effects can be significant if the angle of incidence of outgoing waves is high relative to the flight vehicle wall. These studies are mainly focused on sound propagation from a source that impinges on the airframe fuselage and not from a turbulent source within a boundary layer propagating outwards. Smith and Morfey[39] examined radiation of sound from sources within boundary layers. Their numerical results showed that directivity is dependent on Mach number and boundary layer thickness. Suzuki and Lele[40] found solutions of the Green's function of a third-order convective wave equation using an asymptotic method. Generally, the effect of refraction in the cross-stream direction (normal to the wall) is minimally effected by the meanflow. The predictions within this paper are predominantly in the cross-stream direction. The effects of the meanflow on the propagation of sound waves through the turbulent boundary layer can be taken into account with acoustic analogies such as that of Lilley[41] or Goldstein.[42] These two latter approaches have not yet been used to evaluate the near-field sound and predict the cross-spectrum.

In this paper, we present a theory using the CSAA of Miller,[32] to predict the cross-spectra and auto-spectra of acoustic pressure radiated from the turbulent boundary layer. The source of acoustic radiation considered in this paper is the turbulence within the boundary layer and not an equivalent 'quadrupole' or 'dipole' source on the wall. To exercise the model, a simple self-similar mean flow model is used from which turbulence statistics are estimated. A coherence model is developed based upon the mean flow and turbulence statistics. The wall is accounted for by using the concept of the mirror source originally presented by Powell.[14] Closed-form equations are developed for the cross-spectrum of acoustic pressure, and the associated auto-spectrum is derived from the cross-spectrum.

The remaining portion of this paper discusses the mathematical development of the model. An analysis shows that the developed model is consistent with traditional theory. Finally, predictions compared with measurement and numerical simulations are shown.

Mathematical Theory

We summarize the cross-spectral acoustic analogy then model the two-point cross-correlation of boundary layer turbulence. The resultant equation is simplified through integration and results in a simplified model for cross-spectra and auto-spectra of fluctuating pressure. This model contains arguments of the turbulent statistics and mean flow of the boundary layer. These arguments are examined individually and are approximated from previously developed models or developed here to match a range of measurement data.

Cross-Spectral Acoustic Analogy

The cross-spectral acoustic analogy is derived by Miller[32] and is summarized here briefly. We assume that the Navier-Stokes equations model the physics of boundary layer turbulence and associated acoustics. A partial derivative operator with respect to time and a divergence operator are applied to the continuity and momentum equations, respectively. A wave equation operator with mixed independent values of pressure and density is added to both sides of the difference of the resulting equations. The resultant equation contains the well known Lighthill stress tensor, T_{ij} (see Lighthill[34] for details and discussion of T_{ij}). The right hand side of this equation represents an equivalent aerodynamic source of sound. We express the right hand side terms in expanded form and unlike Lighthill[34] retain all terms. A vector free stream Mach number is introduced to account for an ambient or flight vehicle Mach number, and density is expressed as pressure using the ideal gas law. The equation for pressure is used to form a cross-correlation between two observer points $\boldsymbol{x}$ and $\boldsymbol{x}'$. The theories of Lighthill,[34,43] Ribner,[44] and Ffowcs Williams[45] are used to simplify the resulting spatial cross-correlation of pressure using the assumption that the turbulence is statistically stationary. We group integrand terms according to their relative contribution to the near-field, mid-field, and far-field. Terms with second-order powers in decay correspond to far-field terms, fourth-order powers correspond to mid-field terms, and sixth-order powers correspond to near-field terms. The cross-power spectral density (CPSD) of the fluctuating pressure is then found using a Fourier transform. We find the cross-spectral acoustic analogy of Miller[32]

$$G\left(\boldsymbol{x},\boldsymbol{x}',\omega\right)=\frac{1}{16\pi^2}\int_{-\infty}^{\infty}\ldots\int_{-\infty}^{\infty}\left\{F_{ijlm}\overline{\ddot{T}_{ij}\ddot{T}'_{lm}}+M_{ijlm}\overline{\dot{T}_{ij}\dot{T}'_{lm}}+N_{ijlm}\overline{T_{ij}T'_{lm}}\right\}\times\exp\left[-i\omega\left(\tau+\frac{r}{c_\infty}-\frac{r'}{c_\infty}\right)\right]d\tau d\boldsymbol{\eta}'d\boldsymbol{\eta},\tag{1}$$

where $r=|\boldsymbol{x}-\boldsymbol{y}|+\mathcal{M}_\infty\cdot(\boldsymbol{x}-\boldsymbol{y})$, $\boldsymbol{\eta}=\boldsymbol{\eta}(\xi,\eta,\zeta)$ represents the integration over the source volume that is dependent on $\mathcal{M}_\infty$, and $\mathcal{M}_\infty$ is the vector free-stream Mach number. The prime signifies that the quantity is evaluated at the second position. Note here that r and r' are vector magnitudes and not components. Arguments of the stress tensor are $T_{ij}=T_{ij}\left(\boldsymbol{\eta},\tau\right)$ and dot and double dot of T_{ij} represent the first and second temporal derivatives, respectively. Terms that contribute to the far-field, mid-field, and near-field appear in the integrand and are approximately dependent on r^{-2}, r^{-4}, and r^{-6}, respectively. The far-field term is

$$F_{ijlm}=\frac{r_ir_jr'_lr'_m}{r^2r'^2}\left[\frac{1}{c_\infty^4rr'}\right],\tag{2}$$

the mid-field term is

$$\begin{aligned}M_{ijlm}=&\frac{r_ir_jr'_lr'_m}{r^2r'^2}\left[\frac{9(1-\mathcal{M}_\infty^2)^2}{c_\infty^2r^2r'^2}-\frac{3(1-\mathcal{M}_\infty^2)^2}{c_\infty^2rr'^3}-\frac{3(1-\mathcal{M}_\infty^2)^2}{c_\infty^2r^3r'}\right]-\frac{r_ir_jr'_l}{r^2r'}\left[\frac{6(1-\mathcal{M}_\infty^2)}{c_\infty^2}\left(\frac{2M_{\infty,m}}{r^2r'^2}-\frac{M_{\infty,m}}{rr'^3}\right)\right]\\&-\frac{r_ir'_lr'_m}{rr'^2}\left[\frac{6(1-\mathcal{M}_\infty^2)}{c_\infty^2}\left(\frac{2M_{\infty,j}}{r^2r'^2}-\frac{M_{\infty,j}}{r^3r'}\right)\right]-\frac{r_ir_j}{r^2}\left[\frac{3(1-\mathcal{M}_\infty^2)\delta_{lm}}{c_\infty^2r^2r'^2}+\frac{(1-\mathcal{M}_\infty^2)\delta_{lm}}{c_\infty^2rr'^3}+\frac{2M_{\infty,l}M_{\infty,m}}{c_\infty^2rr'^3}\right]\\&-\frac{r'_lr'_m}{r'^2}\left[\frac{3(1-\mathcal{M}_\infty^2)\delta_{ij}}{c_\infty^2r^2r'^2}+\frac{(1-\mathcal{M}_\infty^2)\delta_{ij}}{c_\infty^2r^3r'}+\frac{2M_{\infty,i}M_{\infty,j}}{c_\infty^2r^3r'}\right]+\frac{r_ir'_l}{rr'}\left[\frac{16M_{\infty,j}M_{\infty,m}}{c_\infty^2r^2r'^2}\right]+\frac{r_i}{r}\left[\frac{4M_{\infty,j}\delta_{lm}}{c_\infty^2r^2r'^2}\right]\\&+\frac{r'_l}{r'}\left[\frac{4M_{\infty,m}\delta_{ij}}{c_\infty^2r^2r'^2}\right]+\frac{\delta_{ij}\delta_{lm}}{c_\infty^2r^2r'^2},\end{aligned}\tag{3}$$

and the near-field term is

$$\begin{aligned}N_{ijlm}=&\frac{r_ir_jr'_lr'_m}{r^2r'^2}\left[\frac{9(1-\mathcal{M}_\infty^2)^4}{r^3r'^3}\right]-\frac{r_ir_jr'_l}{r^2r'}\left[\frac{18M_{\infty,m}(1-\mathcal{M}_\infty^2)^2(1-\mathcal{M}_\infty)^2}{r^3r'^3}\right]\\&-\frac{r_ir'_lr'_m}{rr'^2}\left[\frac{18M_{\infty,j}(1-\mathcal{M}_\infty^2)^2(1-\mathcal{M}_\infty)^2}{r^3r'^3}\right]+\frac{r_ir_j}{r^2}\left[\frac{3(1-\mathcal{M}_\infty^2)^2}{r^3r'^3}\left(2M_{\infty,l}M_{\infty,m}-(1-\mathcal{M}_\infty^2)\delta_{lm}\right)\right]\\&+\frac{r'_lr'_m}{r'^2}\left[\frac{3(1-\mathcal{M}_\infty^2)^2}{r^3r'^3}\left(2M_{\infty,i}M_{\infty,j}-(1-\mathcal{M}_\infty^2)\delta_{ij}\right)\right]+\frac{r_ir'_l}{rr'}\left[\frac{36M_{\infty,j}M_{\infty,m}(1-\mathcal{M}_\infty)^4}{r^3r'^3}\right]\\&-\frac{r_i}{r}\left[\frac{6(1-\mathcal{M}_\infty)^2M_{\infty,j}}{r^3r'^3}\left(2M_{\infty,l}M_{\infty,m}-(1-\mathcal{M}_\infty^2)\delta_{lm}\right)\right]\\&-\frac{r'_l}{r'}\left[\frac{6(1-\mathcal{M}_\infty)^2M_{\infty,m}}{r^3r'^3}\left(2M_{\infty,i}M_{\infty,j}-(1-\mathcal{M}_\infty^2)\delta_{ij}\right)\right]\\&-2(1-\mathcal{M}_\infty^2)\left[\frac{M_{\infty,i}M_{\infty,j}\delta_{lm}}{r^3r'^3}+\frac{M_{\infty,l}M_{\infty,m}\delta_{ij}}{r^3r'^3}\right]+\frac{4M_{\infty,i}M_{\infty,j}M_{\infty,l}M_{\infty,m}}{r^3r'^3}+\frac{(1-\mathcal{M}_\infty^2)^2\delta_{ij}\delta_{lm}}{r^3r'^3}.\end{aligned}\tag{4}$$

To evaluate Eqn. 1 knowledge of $\overline{T_{ij}T'_{lm}}$ and its derivatives must be known. We approximate these three forms of $\overline{T_{ij}T'_{lm}}$ through a single function $\boldsymbol{R}_{ijlm}$ as

$$\overline{T_{ij}T'_{lm}}\approx\boldsymbol{R}_{ijlm},\tag{5}$$

$$\overline{\frac{\partial T_{ij}}{\partial\tau}\frac{\partial T'_{lm}}{\partial\tau'}}\approx\frac{\partial^2\boldsymbol{R}_{ijlm}}{\partial\tau^2},\tag{6}$$

and

$$\overline{\frac{\partial^2T_{ij}}{\partial\tau^2}\frac{\partial^2T'_{lm}}{\partial\tau'^2}}\approx\frac{\partial^4\boldsymbol{R}_{ijlm}}{\partial\tau^4}.\tag{7}$$

These quantities can be calculated using unsteady numerical simulation. In the next section, we approximate them for the wall bounded flow.

Modeling Two-Point Cross-Correlations for Boundary Layer Turbulence

Here, we propose a model for $\boldsymbol{R}_{ijlm}$ for boundary layer turbulence that can be integrated analytically and subsequently produce a simplified model. We propose that $\boldsymbol{R}_{ijlm}$ is separable into the density and Reynolds stress multiplied by a normalized two-point cross correlation as

$$\boldsymbol{R}_{ijlm} = \mathcal{P}_f \overline{\rho}\ \overline{\rho}' \left(\overline{u_i u_j}\ \overline{u_l' u_m'} \right) R, \tag{8}$$

where $\mathcal{P}_f$ is a constant coefficient. The normalized two-point cross-correlation, R, is modeled as

$$R = \exp\left[-\frac{(\xi - \overline{u}\tau)^2}{l_{sx}^2} \right] \exp\left[-\frac{(1 - \tanh[\alpha|\xi|])|\xi - \overline{u}\tau|}{l_{sx}} \right] \exp\left[-\frac{|\xi|}{l_{sx}} \right] \exp\left[-\frac{|\eta|}{l_{sy}} \right] \exp\left[-\frac{|\zeta|}{l_{sz}} \right], \tag{9}$$

where $\overline{u}$ is the local averaged velocity component and α is a constant. The coefficient α, and the hyperbolic tangent term, controls the rate at which R transitions from an exponential function to a Gaussian function. Equations 6 and 7 involve retarded time derivatives that operate on R.

The model for the two-point cross-correlation of the equivalent source must capture the trends observed in measurement. Unfortunately, the task of measuring acoustic sources or their model equivalent is extremely difficult, and usually two-point measurements of pressure and velocity statistics are obtained. Thus, it is not possible to conduct a direct comparison. We illustrate the behavior of the normalized two-point cross-correlation defined in Eqn. 9. For this purpose we select a boundary layer flow with $\mathcal{M}_\infty = 0.50$ and one velocity within the flow of $\overline{u} = 120$ m s^{-1}, as the model varies with $\overline{u}$. A value of α of 10 is adopted here and used throughout the paper, however, this value is only chosen so that it is similar to the measurement of Naka et al.[9] Figure 2 shows the variation of R, governed by Eqn. 9, as a function of τ and ξ, which is the spatial separation between sources in the streamwise direction. The x-axis is normalized by $u_\infty l_{sx}^{-1}$. The streamwise length scale, l_{sx}, is dependent on $\overline{u}$ and $\mathcal{S}t$. The variation of the form of R goes from an exponential decay at $\xi = 0$ to a mixed exponential-Gaussian decay and finally to a fully Gaussian decay at large ξ. The change of transition rate with increasing ξ, from exponential to Gaussian, is dependent on the constant α within Eqn. 9. These decay rates are readily apparent in the models and measurements of Palumbo.[17,46] Unfortunately, the model of Eqn. 9 cannot be directly compared to the measurements of Palumbo[17,46] and Naka et al.[9] because the model is dependent on frequency and local velocity instead of the overall convection velocity deduced from pressure fluctuations at the wall. Nonetheless, it captures the trends observed in measurement.

We isolate the second-order time derivative terms that operate on R and evaluate them as

$$\begin{aligned}
&\frac{\partial}{\partial \tau^2} \exp\left[-\frac{(\xi - \overline{u}\tau)^2}{l_{sx}^2} \right] \exp\left[-\frac{(1 - \tanh[\alpha|\xi|])|\xi - \overline{u}\tau|}{l_{sx}} \right] \\
&\qquad = \frac{2\overline{u}^2}{l_{sx}^2} \exp\left[-\frac{(\xi - \overline{u}\tau)^2}{l_{sx}^2} - \frac{|\overline{u}\tau - \xi|(1 - \tanh[\alpha|\xi|])}{l_{sx}} \right] \\
&+ \exp\left[-\frac{(\xi - \overline{u}\tau)^2}{l_{sx}^2} - \frac{|\overline{u}\tau - \xi|(1 - \tanh[\alpha|\xi|])}{l_{sx}} \right] \left(\frac{2\overline{u}(\xi - \overline{u}\tau)}{l_{sx}^2} - \frac{\Delta_1(1 - \tanh[c_1|\xi|])}{l_{sx}} \right)^2,
\end{aligned} \tag{10}$$

where $\Delta_1 = -\overline{u}$ for $-\xi + \overline{u}\tau \leq 0$ and is otherwise $\overline{u}$. The fourth-order time derivative operating on R is

$$\begin{aligned}
&\frac{\partial}{\partial \tau^4} \exp\left[-\frac{(\xi - \overline{u}\tau)^2}{l_{sx}^2} \right] \exp\left[-\frac{(1 - \tanh[\alpha|\xi|])|\xi - \overline{u}\tau|}{l_{sx}} \right] \\
&\qquad = \frac{12\overline{u}^4}{l_{sx}^4} \exp\left[-\frac{(\xi - \overline{u}\tau)^2}{l_{sx}^2} - \frac{|\overline{u}\tau - \xi|(1 - \tanh[\alpha|\xi|])}{l_{sx}} \right] \\
&- \frac{12\overline{u}^2}{l_{sx}^2} \exp\left[-\frac{(\xi - \overline{u}\tau)^2}{l_{sx}^2} - \frac{|\overline{u}\tau - \xi|(1 - \tanh[\alpha|\xi|])}{l_{sx}} \right] \left(\frac{2\overline{u}(\xi - \overline{u}\tau)}{l_{sx}^2} - \frac{\Delta_1(1 - \tanh[\alpha|\xi|])}{l_{sx}} \right)^2 \\
&+ \exp\left[-\frac{(\xi - \overline{u}\tau)^2}{l_{sx}^2} - \frac{|\overline{u}\tau - \xi|(1 - \tanh[\alpha|\xi|])}{l_{sx}} \right] \left(\frac{2\overline{u}(\xi - \overline{u}\tau)}{l_{sx}^2} - \frac{\Delta_1(1 - \tanh[\alpha|\xi|])}{l_{sx}} \right)^4.
\end{aligned} \tag{11}$$

We approximate the subsequent integration of the model equation involving terms dependent on τ. The first term within Eqn. 11 is dominant because of the presence of $\overline{u}^4$, which is large for relatively high Reynolds number flows that are fully turbulent. Note that the far-field term contains a power involving $\overline{u}^2$,

and this power is of the same magnitude of the dominant power within the mid-field term. However, as the sources have been separated into their respective far-field, mid-field, and near-field components, only the most dominant power in each term is important and not the relative powers between terms. We isolate and integrate terms involving τ within Eqns. 1, 9, 10, and 11. These integrations are written as a conditional statement and subsequent relations as

$$\mathcal{I}_{\tau 4} = \frac{12\overline{u}^4}{l_{sx}^4} \int_{-\infty}^{\infty} \exp\left[-\frac{(\xi-\overline{u}\tau)^2}{l_{sx}^2} - \frac{|\overline{u}\tau-\xi|(1-\tanh[\alpha|\xi|])}{l_{sx}}\right] \exp\left[-i\omega\tau\right] d\tau$$

$$= \frac{6\pi^{1/2}\overline{u}^3}{l_{sx}^3} \exp\left[\frac{\overline{u}^2 - 2i\overline{u}l_{sx}\omega - 4\pi i\overline{u}\omega - l_{sx}^2\omega^2}{4\overline{u}^2}\right] \begin{cases} \exp\left[\frac{\overline{u}\tanh[\alpha\xi](-2(\overline{u}+il_{sx}\omega)+\overline{u}\tanh[\alpha\xi])}{4\overline{u}^2}\right] \\ \times \left(\exp\left[\frac{il_{sx}\omega\tanh[\alpha\xi]}{\overline{u}}\right]\operatorname{erfc}\left[\frac{\overline{u}-il_{sx}\omega-\overline{u}\tanh[\alpha\xi]}{2\overline{u}}\right]\right. \\ \left. + \exp\left[\frac{il_{sx}\omega}{\overline{u}}\right]\operatorname{erfc}\left[\frac{\overline{u}+il_{sx}\omega-\overline{u}\tanh[\alpha\xi]}{2\overline{u}}\right]\right) & \text{for } \xi \geq 0 \\ \text{and} \\ \exp\left[\frac{\overline{u}\tanh[\alpha\xi](2(\overline{u}-il_{sx}\omega)+\overline{u}\tanh[\alpha\xi])}{4\overline{u}^2}\right] \\ \times \left(\operatorname{erfc}\left[\frac{\overline{u}-il_{sx}\omega+\overline{u}\tanh[\alpha\xi]}{2\overline{u}}\right]\right. \\ \left. + \exp\left[\frac{il_{sx}\omega(1+\tanh[\alpha\xi])}{\overline{u}}\right]\operatorname{erfc}\left[\frac{\overline{u}+il_{sx}\omega+\overline{u}\tanh[\alpha\xi]}{2\overline{u}}\right]\right) & \text{for } \xi < 0 \end{cases} \tag{12}$$

and

$$\mathcal{I}_{\tau 2} = \frac{l_{sx}^2}{6\overline{u}^2}\mathcal{I}_{\tau 4} \quad \text{and} \quad \mathcal{I}_{\tau 0} = \frac{l_{sx}^4}{12\overline{u}^4}\mathcal{I}_{\tau 4}. \tag{13}$$

Equation 12 is found using insight from integration tables (see Zwillinger[47]). Using $\mathcal{I}_{\tau 0}$, $\mathcal{I}_{\tau 2}$, and $\mathcal{I}_{\tau 4}$, Eqn. 1 is written

$$G(\boldsymbol{x},\boldsymbol{x}',\omega) = \frac{\mathcal{P}_f}{16\pi^2} \int_{-\infty}^{\infty} \ldots \int_{-\infty}^{\infty} \overline{\rho}\,\overline{\rho}'\overline{u_i u_j}\;\overline{u_l' u_m'}\left\{F_{ijlm}\mathcal{I}_{\tau 4} + M_{ijlm}\mathcal{I}_{\tau 2} + N_{ijlm}\mathcal{I}_{\tau 0}\right\} \times \exp\left[-i\omega\left(\frac{r}{c_\infty} - \frac{r'}{c_\infty}\right)\right] d\boldsymbol{\eta}' d\boldsymbol{\eta}. \tag{14}$$

If the auto-spectral solution of the acoustic pressure is desired then Eqn. 14 can be simplified through analytical integration after equating $\boldsymbol{x} = \boldsymbol{x}'$. We obtain

$$S(\boldsymbol{x},\omega) \approx \frac{\mathcal{P}_f}{4\pi^2} \int_{-\infty}^{\infty} \ldots \int_{-\infty}^{\infty} \overline{\rho}\,\overline{\rho}'\overline{u_i u_j}\;\overline{u_l' u_m'} l_{sy} l_{sz}\left\{F_{ijlm}\mathcal{I}_{\tau 4} + M_{ijlm}\mathcal{I}_{\tau 2} + N_{ijlm}\mathcal{I}_{\tau 0}\right\} d\xi d\boldsymbol{\eta}. \tag{15}$$

Equations 14 and 15 are closed-form integral equations for the cross-spectrum and auto-spectrum of the acoustic pressure in the domain outside the turbulent boundary layer. The spatially varying coherence as a function of ω of the acoustic pressure, Γ, is

$$\Gamma(\boldsymbol{x},\boldsymbol{x}',\omega) = \frac{G(\boldsymbol{x},\boldsymbol{x}',\omega)\,G^*(\boldsymbol{x},\boldsymbol{x}',\omega)}{G(\boldsymbol{x}_1,\boldsymbol{x}_1,\omega)\,G(\boldsymbol{x}',\boldsymbol{x}',\omega)}, \tag{16}$$

where G is defined in Eqn. 14. Note that $\Gamma = 1$ when $\boldsymbol{x} = \boldsymbol{x}'$.

Turbulent Mean Flow

Here, we develop simple models to approximate the arguments of the developed acoustic model. For the purpose of demonstrating the validity of the approach, we restrict our effort to turbulent boundary layers with no pressure gradient and with an adiabatic wall. The mean flow and statistics of turbulence can easily be found through contemporary numerical techniques or alternatively with an embedded function method such as that of Degani et al.[48] Here, to demonstrate the newly developed method only, we attempt to

approximate the mean flow and turbulent statistics through simplified analytical formulae that are based upon observations or numerical simulation. We entirely characterize the turbulent flow-field by specifying the Reynolds number, $\mathcal{R}e_x$, and the free-stream Mach number, $\mathcal{M}_\infty$. The axial location of the turbulent field, x_l, corresponding to $\mathcal{R}e_x$ and $\mathcal{M}_\infty$ is estimated by Schlichting[6] as $x_l \approx \mathcal{R}e_x \nu_\infty u_\infty^{-1}$, where $u_\infty = \mathcal{M}_\infty c_\infty^{-1}$. The skin friction estimated by Schlichting[6] is

$$c_f \approx 2\left(\frac{\kappa}{\log \mathcal{R}e_x} G(\log \mathcal{R}e_x)\right)^2, \tag{17}$$

where $G(\log Re_x)$ is a function that approaches unity as $\mathcal{R}e_x$ approaches infinity and is approximately 1.45 in the range of $1\times10^5 < Re_x < 1\times10^6$. The wall shear stress is $\tau_w = \frac{1}{2} c_f \rho_\infty u_\infty^2$. The displacement thickness is defined as

$$\delta = \int_0^\infty \left(1 - \frac{\rho}{\rho_\infty}\frac{u}{u_\infty}\right) dy \tag{18}$$

and is approximated

$$\delta \approx \frac{7}{50}\frac{\nu_\infty}{u_\infty}\frac{Re_x}{\log Re_x} G(\log Re_x) \tag{19}$$

for initialization of the mean flow only. The wall friction velocity is $u_\tau = \left(\tau_w \rho_\infty^{-1}\right)^{1/2}$. The wall coordinate is $y^+ = u_\tau y \nu^{-1}$. We adopt the composite boundary layer model of Musker[49] for $u^+ = u u_\tau^{-1}$ combined with Coles[50] law of the wake

$$\begin{aligned} u^+_{\text{incompressible}} = {} & \frac{1}{\kappa}\log\left[\frac{y^+ - c_a}{-c_a}\right] + \frac{c_R^2}{(c_a(4c_\alpha - c_a))} \\ & + \left\{\frac{c_R^2}{(c_a(4c_\alpha - c_a))}\log\left[-\frac{c_a\left((y^+ - c_\alpha)^2 + c_\beta^2\right)^{1/2}}{c_R(y^+ - c_a)}\right]\right. \\ & \left. + \frac{c_\alpha}{c_\beta}(4c_\alpha + 5c_a)\left(\arctan\left[\frac{(y^+ - c_\alpha)}{c_\beta}\right] + \arctan\left[\frac{c_\alpha}{c_\beta}\right]\right)\right\} \\ & + \frac{\Pi}{\kappa}\left(1 - \cos\left[\frac{\pi y}{\delta}\right]\right), \end{aligned} \tag{20}$$

where $c_a = -10.3061$, $c_\alpha = (-\kappa^{-1} - c_a)/2$, $c_\beta = (-2c_a c_\alpha - c_\alpha^2)^{1/2}$, $c_R = (c_\alpha^2 + c_\beta^2)^{1/2}$, and κ is the von Karman coefficient. The wake factor of Coles,[50] Π, is found implicitly by enforcing $u^+ u_\tau = u_\infty$ at δ, which is calculated after evaluating Eqn. 20. To account for the compressibility effects within the flow we adopt the van Driest transform as shown by Huang and Coleman[51] that modifies $u^+_{\text{incomp.}}$ as

$$u^+ = \frac{u_\infty}{2u_\tau a^2}\left(Q\sin\left[\frac{a u_\tau}{u_\infty}u^+_{\text{incomp.}} - \arcsin\left[bQ^{-1}\right]\right] + b\right), \tag{21}$$

where $a = \left(R_c \frac{\gamma-1}{2}\mathcal{M}_\infty^2 \frac{T_\infty}{T_w}\right)^{1/2}$, $b = T_{aw}T_w^{-1} - 1$, $T_{aw} = T_\infty(1 + R_c\frac{\gamma-1}{2}\mathcal{M}_\infty^2)$, and $Q = (b^2 + 4a^2)^{1/2}$. The subscript 'aw' stands for adiabatic wall temperature and the subscript 'w' denotes a quantity at the wall. When the van Driest transform is used then τ_w and dependent variables are modified iteratively to match the chosen $\mathcal{M}_\infty$. Changes of τ_w and dependent values are very small relative to the originally prescribed values. The variation of temperature within the boundary layer is approximated using the model of Walz[52]

$$\frac{T}{T_\infty} = 1 + \frac{R_c\mathcal{M}_\infty^2(\gamma-1)}{2}\left[1 - \left(\frac{\overline{u}}{u_\infty}\right)^2\right], \tag{22}$$

where $R_c = 0.89$ is the recovery factor. The variation of density is found through the ideal gas law.

The validity of Eqn. 21 has been well established for fully turbulent high Reynolds number boundary layers with no pressure gradient that are attached to solid smooth walls. We compare Eqn. 21 to the mean flow predicted by the LES of Gloerfelt and Berland,[30] the DNS of Jimenez et al.,[53] and the measurement of Erm and Joubert.[54] Note that the LES of Gloerfelt and Berland[30] contains associated acoustic predictions, and this case represents the main validation for the developed acoustic prediction technique. Thus, it is

important that Eqn. 21 and the results of Gloerfelt and Berland[30] are in good agreement. This comparison is shown in Fig. 3, where the y-axis is u^+ and the x-axis is y^+. The composite profile of u^+, with the van Driest correction, is shown as a solid line, and the other data are shown as various dashed or dotted lines. Here, predicted and numerical profiles are at $\mathcal{M}_\infty = 0.50$ and $\mathcal{R}e = 1551$, and the measured profile is at $\mathcal{R}e = 1568$. The composite profile, predictions, and measurement satisfy $u^+ = 1$ at $y^+ = 1$. A viscous sublayer, log-law region, and the effect of Coles[50] wake factor are present within the composite profile at approximately $1 < y^+ < 10$, $30 < y^+ < 300$, and $300 < y^+ < 800$, respectively. In the free-stream region, scaling u^+ by u_τ recovers the prescribed free-stream value of u_∞ exactly, as an iterative process was used to find Coles wake factor, Π. This composite profile is independent with variation of $\mathcal{R}e$, captures compressibility effects, but does not account for a pressure gradient, permeability of the wall, or surface roughness. The comparison is for illustrative purposes and to demonstrate that our implementation is satisfactory.

Turbulent Length Scale

We estimate the length scale within R (Eqn. 9) by adopting the model of Efimtsov[16]

$$l_s = a_4 \delta \left[\left(\frac{a_1 2\pi f}{u_c} \right)^2 + \frac{a_2^2}{\left(\frac{2\pi f \delta}{u_\tau} \right)^2 + \left(\frac{a_2}{a_3} \right)^2} \right]^{-\frac{1}{2}}, \tag{23}$$

where $a_1 = 0.1$, $a_2 = 72.8$, $a_3 = 1.54$, and $a_4 = 6$. The spanwise length scale uses an alternative set of coefficients, $a_1 = 0.77$, $a_2 = 548$, and $a_3 = 13.5$. These coefficients correspond to those calibrated by Efimtsov[16] based on wind-tunnel data. The coefficient a_4 was set to match the simulations of Gloerfelt and Margnat.[31] Palumbo[17,46] showed that these coefficients do not necessarily match those that are calibrated based upon flight test data. He presented an alternative set of coefficients that can be used to match full-scale free-stream data. The requirement for an alternative set of coefficients comes as no surprise given the large differences between wind-tunnel measurements of flat plate turbulent boundary layers and aircraft in flight, where there is strong curvature of the fuselage and axial pressure gradients.

We now examine the variation of the turbulent length scale as a function of frequency in outer coordinates. A turbulent boundary layer has properties $\mathcal{R}e_x = 1 \times 10^6$, $\mathcal{M}_\infty = 0.70$, and at x_l the boundary layer thickness is $\delta \approx 9.555 \times 10^{-4}$ m. The variation of the streamwise length scale is calculated with Eqn. 23 by using the streamwise coefficients. The result is the variation of l_{sx} as a function of frequency and $y\delta^{-1}$. Figure 4 shows $l_{sx}\delta^{-1}$ at three frequencies corresponding to $\mathcal{S}t \approx 0.4$, 4, and 40. Variations of l_{sx} at these frequencies show relatively the same behavior near the wall as they approach zero. At high frequencies the model approaches constant values with increasing y and should decay well within the free-stream, though this is not a concern acoustically as we are interested in boundary layer turbulence and restrict integration within $y < \delta$. The predicted length scale generally follows the same trends shown by Efimtsov,[16] in that the maximum length scale is very small at low frequencies, increases to a maximum at mid frequencies, and again decreases at high frequencies. This trend is similar to the wavenumber spectrum of turbulent length scales. We cannot directly compare this form of the length scale model with measurements of wall based-length scales, such as with the results of Naka et al.,[9] as the length scale varies spatially within the boundary layer. Recall that the length scales based upon wall pressure fluctuations are highly correlated with the pressure fluctuations within the fluid and their coherence. Thus this crude model will likely yield more physical results and is likely better than the simpler approximation of $l_{sx} \approx y$ multiplied by constant. A superior method would use numerical simulation such as steady RANS, but our aim is to develop a simpler model that evaluates in seconds to demonstrate the validity of the overall approach.

Turbulent Reynolds Stress

Equation 8 contains arguments of the Reynolds stress. Here, we develop a model for the diagonal terms of the Reynolds stress tensor and base the off-diagonal terms on the diagonal terms. The measurements of Duan et al.[55] are used for calibration of the model. Unfortunately, similarity of $\overline{u'u'}$ has not been established in the present literature, but the maximum of $(\overline{u'u'})^{1/2} u_\tau^{-1}$ within a boundary layer at large $\mathcal{M}_\infty$ approaches an asymptote within a small region of $y\delta^{-1}$. In the outer region of the boundary layer the

scaling of $(\overline{u'u'})^{1/2}u_\tau^{-1}$ with $\mathcal{M}_\infty$ decreases with $\mathcal{M}_\infty$. Thus, we model $(\overline{u'u'})^{1/2}u_\tau^{-1}$ using a summation of two log-normal distributions in an attempt to capture these two trends. We propose

$$\begin{aligned}&\frac{\overline{u'u'}^{1/2}}{u_\tau}\left(0.45\exp\left[-\log[\mathcal{M}_\infty+2]+2.1\right]\right)^{-1}\\&=\begin{cases}c_4\exp\left[-\frac{(\log[y\delta^{-1}]-\log[c_1])^2}{2c_2^2}\right]+c_8\exp\left[-\frac{(\log[y\delta^{-1}]-\log[c_5])^2}{2c_6^2}\right] & \text{for } \log[y\delta^{-1}]-\log[c_1]\le 0\\ c_4\exp\left[-\frac{(\log[y\delta^{-1}]-\log[c_1])^2}{2c_3^2}\right]+c_8\exp\left[-\frac{(\log[y\delta^{-1}]-\log[c_5])^2}{2c_7^2}\right] & \text{for } \log[y\delta^{-1}]-\log[c_1]>0,\end{cases}\end{aligned} \tag{24}$$

where $c_1 = 0.037$, $c_2 = 0.60$, $c_3 = 0.60$, $c_4 = 0.8$, $c_5 = 0.037$, $c_6 = 0.60$, $c_7 = 3 - 0.10318\mathcal{M}_\infty$, and $c_8 = 1.7$. Similar relations can be developed for $(\overline{v'v'})u_\tau^{-1}$ and $(\overline{w'w'})u_\tau^{-1}$. Fortunately, this is not necessary because in the high Mach number limit $\overline{v'v'}^{1/2}\overline{u'u'}^{-1/2}$ and $\overline{w'w'}^{1/2}\overline{u'u'}^{-1/2}$ are only dependent on $y\delta^{-1}$, except for some relatively minor additional anisotropy. By defining these ratios as a summation of two log-normal distributions, we can easily calculate $\overline{v'v'}^{1/2}$ and $\overline{w'w'}^{1/2}$ with knowledge of Eqn. 24. We propose that the ratio $\overline{v'v'}^{1/2}\overline{u'u'}^{-1/2}$ is

$$\frac{\overline{v'v'}^{1/2}}{\overline{u'u'}^{1/2}} = 1 - c_{v3}\exp\left[-\frac{\log[y\delta^{-1}-c_{v1}]^2}{2c_{v2}^2}\right] + \left(1 - c_{v6}\exp\left[-\frac{\log[y\delta^{-1}-c_{v4}]^2}{2c_{v5}^2}\right]\right) - 1, \tag{25}$$

where $c_{v1} = -3.54046$, $c_{v2} = 0.93$, $c_{v3} = 0.595$, $c_{v4} = -0.693147$, $c_{v5} = 1.25$, and $c_{v6} = 0.22$. Similarly for $\overline{w'w'}^{1/2}\overline{u'u'}^{-1/2}$

$$\frac{\overline{w'w'}^{1/2}}{\overline{u'u'}^{1/2}} = 1 - c_{w3}\exp\left[-\frac{\log[y\delta^{-1}-c_{w1}]^2}{2c_{w2}^2}\right] + \left(1 - c_{w6}\exp\left[-\frac{\log[y\delta^{-1}-c_{w4}]^2}{2c_{w5}^2}\right]\right) - 1, \tag{26}$$

where $c_{w1} = -4.00653$, $c_{w2} = 1.50$, $c_{w3} = 0.910$, $c_{w4} = -0.579818$, $c_{w5} = 1.85$, and $c_{w6} = 0.26$. The coefficients of Eqns. 24 through 26 were calibrated initially by intuition and then slight changes were made until the model matched the experiment. The root mean square of v' and w' are found through the relations

$$\overline{v'v'}^{1/2} = \left(\frac{\overline{v'v'}^{1/2}}{\overline{u'u'}^{1/2}}\right)\overline{u'u'}^{1/2} \quad \text{and} \quad \overline{w'w'}^{1/2} = \left(\frac{\overline{w'w'}^{1/2}}{\overline{u'u'}^{1/2}}\right)\overline{u'u'}^{1/2}. \tag{27}$$

Figure 5 shows the comparison between Eqn. 24 and the measurements of Duan et al.[55] The y-axis is $(\overline{u'u'})^{1/2}$ normalized by u_τ and the x-axis is $y\delta^{-1}$. The model is evaluated at various $\mathcal{M}_\infty$ and labeled accordingly. Equation 24 is essentially the summation of two log-normal distributions that scale with $\mathcal{M}_\infty$. Corresponding measurements at $\mathcal{M}_\infty$ of Duan et al.[55] are shown using the same line type but with an additional symbol. Measurements were performed by Duan et al.[55] over a range of compressible Mach numbers from 0.30 to 11.93. Unfortunately, a collapse based on a combination of flow parameters is difficult to obtain. The maximum magnitude of $(\overline{u'u'})^{1/2}$ occurs near $y\delta^{-1} \approx 0.03$, and the location of the maximum remains constant with increasing $\mathcal{M}_\infty$. When normalized by u_τ, this magnitude approaches $(\overline{u'u'})^{1/2}u_\tau^{-1} \approx 2.4$ as $\mathcal{M}_\infty$ increases. Near the edge of the boundary layer there is no consistent asymptotic behavior of $(\overline{u'u'})^{1/2}$ as $\mathcal{M}_\infty$ increases. To account for this trend, within the range of $0.01 \le \mathcal{M}_\infty \le 12$, the argument of the log-normal distribution is scaled by a factor of $-0.10318\mathcal{M}_\infty + 3$, as shown in Eqn. 24. The empirical model for $(\overline{u'u'})^{1/2}$ compares quite satisfactorily given the difficulty and uncertainty of these measurements.

Like $(\overline{u'u'})^{1/2}u_\tau^{-1}$, similarity of $(\overline{v'v'})^{1/2}u_\tau^{-1}$ and $(\overline{w'w'})^{1/2}u_\tau^{-1}$ with varying $y\delta^{-1}$ remains elusive within turbulent boundary layers. However, $(\overline{v'v'})^{1/2}(\overline{u'u'})^{-1/2}$ and $(\overline{w'w'})^{1/2}(\overline{u'u'})^{-1/2}$ quickly approach asymptotic values dependent on $y\delta^{-1}$ as $\mathcal{R}e$ increases. Figures 6 and 7 show these ratios as a function of $y\delta^{-1}$. Predictions of Eqn. 25 are shown in Fig. 6, and predictions of Eqn. 26 are shown in Fig. 7. We observe a minimum of $(\overline{v'v'})^{1/2}(\overline{u'u'})^{-1/2}$ near $y\delta^{-1} \approx 0.03$ and a minimum of $(\overline{w'w'})^{1/2}(\overline{u'u'})^{-1/2}$ near $y\delta^{-1} \approx 0.02$. Recall that both of these models consist of summations of log-normal distributions, where the first controls the behavior near the wall and the second controls the behavior in the outer region. Their effect is apparent in the approximate ranges of $0.01 < y\delta^{-1} < 0.1$ and $0.1 < y\delta^{-1}$, respectively. In both Eqns. 25 and 26, we have enforced the result to approach unity as $y\delta^{-1}$ approaches zero. Measurements are not available very close to the wall, thus the forms of the ratios of the Reynolds stresses contain some assumption regarding their near-wall behavior. Note that the $(\overline{v'v'})^{1/2}$ component approaches unity faster relative to $(\overline{w'w'})^{1/2}$.

Note that the turbulent kinetic energy is $k = \frac{1}{2}\overline{u_i' u_i'}$. To obtain the off-diagonal Reynolds stress components we turn to classical theory. Early models for Reynolds stress are based on the eddy viscosity hypothesis, $-\rho\overline{u'v'} \approx \nu_\tau \partial\overline{u}/\partial y$ and the eddy viscosity is estimated as $\nu_t \approx \rho l^2 \left|\partial\overline{u}/\partial y\right|$. Thus, we approximate the off-diagonal term as $-\overline{u'v'} \approx l_{sx}^2 (\partial\overline{u}/\partial y)^2$. It is very difficult to model the off-diagonal terms as clear trends are not known in the literature, thus we approximate them as small fractions of $\overline{u'v'}$. We have now developed a closed prediction equation and associated arguments that are based upon current theory and measurements of zero pressure gradient turbulent boundary layers.

Analysis

By examining the model equation for spectral density of acoustic pressure in Eqn. 15 (by setting $\boldsymbol{x} = \boldsymbol{x}'$), it is argued that $S \propto \overline{\rho}\ \overline{\rho' \overline{u_i u_j}}\ \overline{u_l' u_m'} l_{sy} l_{sz} \left\{F_{ijlm}\mathcal{I}_{\tau 4} + M_{ijlm}\mathcal{I}_{\tau 2} + N_{ijlm}\mathcal{I}_{\tau 0}\right\} d\xi d\boldsymbol{\eta}$. We approximate the Reynolds stress by its most dominant component, $\overline{u'u'}^{1/2} \propto u_\tau \left(0.45 \exp\left[-\log[\mathcal{M}_\infty + 2] + 2.1\right]\right)$, as shown in Eqn. 24. Other diagonal components of the Reynolds stress scale as $\overline{u'u'}^{1/2}$, and the off-diagonal components that are smaller in magnitude and negative, are neglected. The term, $\left(0.45 \exp\left[-\log[\mathcal{M}_\infty + 2] + 2.1\right]\right)$, for the scaling of the first diagonal component of the Reynolds stress represents a relatively weak correction to account for the slight amplitude decrease of Reynolds stress as Mach number increases. Now, with the definition of $u_\tau = (\tau_w \rho_w^{-1})^{1/2}$, and examining the relation for τ_w, it is reasonable to assume $\tau_w \propto c_f \rho_\infty u_\infty^2$. The skin friction, as shown in Eqn. 17, is approximated as $c_f \propto \left(\kappa G(\log \mathcal{R}e_x)/\log \mathcal{R}e_x\right)^2$. Using these relations we argue that $\overline{\rho}\ \overline{\rho' \overline{u_i u_j}}\ \overline{u_l' u_m'} \propto \overline{\rho}^2 (c_f \rho_\infty \rho_w^{-1} u_\infty^2)^2$. The far-field, mid-field, and near-field terms, as shown in Eqns. 2 through 4, scale as $F_{ijlm} \propto c_\infty^{-4} r^{-2}$, $M_{ijlm} \propto c_\infty^{-2} r^{-4}$, and $N_{ijlm} \propto r^{-6}$, respectively. Terms resulting from integration involving τ, as shown in Eqns. 12 and 13, scale as $\mathcal{I}_{\tau 4} \propto \overline{u}^4 l_{sx}^{-4} \tau_s$, $\mathcal{I}_{\tau 2} \propto \overline{u}^2 l_{sx}^{-2} \tau_s$, and $\mathcal{I}_{\tau 2} \propto \tau_s$, respectively. Here, τ_s is a time scale of turbulence. By examining Eqn. 23, it is argued that the length scale varies as $l_s \propto \delta$. The differentials within the approximation of S are representative of a volumetric integral, and we write $\boldsymbol{\eta} \propto V$, where V is the differential volume of the boundary layer turbulence. Recall that integration of the model equation with respect to ξ resulted in a term involving l_s, thus we approximate the integrals with respect to ξ and η as l_s, where l_s is proportional to δ and η is proportional to V. Using these arguments we find a simplified scaling argument for the spectral density of acoustic pressure

$$S \propto c_f^2 \overline{\rho}^2 \left(\frac{\rho_\infty}{\rho_w}\right)^2 u_\infty^4 l_{sx} l_{sy} l_{sz} \tau_s \left\{\frac{\overline{u}^4}{c_\infty^4 r^2 l_{sx}^4} + \frac{\overline{u}^2}{c_\infty^2 r^4 l_{sx}^2} + \frac{1}{r^6}\right\} V. \tag{28}$$

Now, we assume that $l_{sx} \propto l_{sy} \propto l_{sz} \propto \delta$, $\overline{u} \propto u_\infty$, and that the observer is in the far-field. Recall that we have defined the turbulent kinetic energy as $k = \frac{1}{2}\overline{u_i' u_i'}$. We estimate the turbulent time scale given knowledge of l_{sx} in Eqn. 23 and k using Eqns. 24, 25, and 26, with the one-point estimation $\tau_s \approx c_\tau l_s k^{-1/2}$, where c_τ is a constant near unity. We find a simplified scaling of spectral density of acoustic pressure in the far-field from a turbulent boundary layer

$$S_{\text{far-field}} \propto \frac{c_f^2}{c_\infty^4 r^2} \frac{\tau_s}{\delta} \left(\frac{\overline{\rho}\rho_\infty}{\rho_w}\right)^2 u_\infty^8 V. \tag{29}$$

Implementation

The numerical evaluation of Eqn. 14 is complex. Here we describe an approach for its evaluation and associated coordinate system. Equations 14 and 15 do not account for wave interaction with the wall that bounds the flow. To account for the wall, we adopt the approach used by Powell,[14] who used the concept of the 'mirror' source. Eqn. 14 requires the knowledge of two observer positions, two source positions, and associated vectors dependent on the observer and source positions. This requirement results in three situations that are illustrated in Fig. 8. Figure 8 shows the coordinate system of the boundary layer flow aeroacoustics problem, where x is the streamwise direction, y is the cross-stream direction, and z is the spanwise direction. The leading edge of the plate is located at $x = 0$, centered about $y = 0$ and $z = 0$, and x_l resides on the positive x-axis. Two shaded areas of Fig. 8 represent the edges of the plate in the spanwise direction. Within each sub-figure two observers, $\boldsymbol{x}$ and $\boldsymbol{x}'$, are shown at two separate spatial locations for illustrative purposes. Observer positions are restricted to $y > \delta$, and δ is a function of x. Source positions, which are separated by the vector $\boldsymbol{\eta}$, are shown for each observer. Sources must be within the turbulent

flow-field and are restricted to $|y| \leq \delta$, where the absolute value is due to the use of the mirror source concept. Radiation vectors, from each source to each observer, are shown as $\boldsymbol{r}$ and $\boldsymbol{r}'$. By examining Eqn. 14, it is evident that for every source position $\boldsymbol{y}$, the vector $\boldsymbol{\eta}$ is defined to include every possible source location $\boldsymbol{y}'$. Figure 8(a), 8(b), and 8(c) illustrate three situations where both source positions are within $y > 0$, where both sources are within $y < 0$, and where a source is above and below $y = 0$, respectively. Sources can not exist within the $x - z$ plane because the turbulent kinetic energy is zero. That is, we are interested in the noise from the turbulent flow. There exists a propagation delay of acoustic radiation from the mirrored sources, though they share the same equivalent acoustic source. For example, the time delay for a source located above the wall and another below the wall is relatively large compared to when they are on the same side of the wall. The increase of time delay, τ, has the effect of lowering the coherence between sources.

We evaluate Eqns. 14 and 15 numerically, and here the algorithm is described. One prescribes $\mathcal{R}e_x$, $\mathcal{M}_\infty$, observer positions, plate span and length, and frequencies. Based on knowledge of $\mathcal{R}e_x$ and $\mathcal{M}_\infty$ the quantities x_l, c_f, τ_w, δ, u_τ, y^+, and $\mathcal{R}e_\tau$ are subsequently found. For the purpose of numerical integration, the number of points used to resolve the boundary layer is approximated as $8\delta(y^+)^{-1}$. These points are distributed evenly from $y = 0$ to 2δ. Values of u^+ (Eqn. 21) at discrete points within the boundary layer, y, and as a function of streamwise location, x, are calculated. Coles wake factor, Π (within Eqn. 20), is found iteratively in conjunction with the van Driest transformation. Successive iteration for Π stops when Π from the current iteration is less than 0.01 percent different from the previous iteration and u_∞ is within 0.01 percent error of u_∞ specified initially. The temperature and density profiles are calculated at each axial location. Streamwise dependent parameters, such as the momentum thickness, θ, are calculated using numerical integration in the cross-stream direction. Predictions are conducted for each set of observer positions, $\boldsymbol{x}$ and $\boldsymbol{x}'$, and frequencies of interest, ω. During each iteration, length scales, turbulent statistics, and the integrals $\mathcal{I}_i$ are evaluated. Spatial integrals of Eqns. 14 and 15 are evaluated numerically using the trapezoidal rule. The boundary layer is resolved spatially by discretizing it with equally spaced points. The spacing of points is equal to the distance from the wall to the location corresponding to $y^+ = 1$. Doubling the number of points resulted in a maximum change in the predicted sound pressure level of 0.01 dB, which is well within engineering accuracy. The double summation involving m and n from one to three enclosing the integrand of Eqns. 14 and 15 is evaluated for each combination of observer position, frequency, and iteration. Near-field, mid-field, and far-field terms are accounted for separately in the calculation of S, and they are subsequently summed together for the total spectral density. With this approach each component can be examined individually. Finally, coherence is calculated using Eqn. 16.

Aeroacoustic Results

This section presents results that are based upon the newly developed model and associated arguments. Acoustic predictions are compared with numerical simulation, and an example near-field prediction of the sound power is shown. Finally, the scaling of the total acoustic energy is investigated with respect to variation of $\mathcal{M}_\infty$.

We now examine the statistics of the predicted acoustic radiation from a turbulent boundary layer. Unfortunately, the availability of high quality measurement data of the acoustic radiation from a turbulent boundary layer on flat plates is understandably almost absent. This is because by nature it is of low-intensity, and within wind-tunnels or other experimental apparatus the acoustic field is contaminated by sound from other sources. Perhaps one of the best experiments to measure solely the sound from turbulent boundary layers was performed by Greshilov and Mironov,[20] but their measurements contained noise from many other sources, did not capture the correct scaling, and are limited to very small velocities near 10 m s^{-1}. We are forced to compare our approach with DNS or LES solutions of turbulent boundary layer flow. These simulations must fully resolve the acoustics and aerodynamics of the flow-field. Recently, a series of papers by Gloerfelt and colleagues examined the turbulent boundary layer and associated acoustic radiation. We use their results to validate Eqn. 15. For details of these simulations the reader is directed to Gloerfelt et al.[30,31,56,57]

We compare predictions of spectral density governed by Eqn. 15 in conjunction with the simplified aerodynamic model of the turbulent boundary layer with the LES simulations of Gloerfelt and Margnat.[31] A substantial effort was made to match the conditions of the numerical simulations of Gloerfelt and Margnat.[31] Recall that the developed mean flow model and associated turbulent statistics are for a turbulent boundary layer on a flat plate. In the large-eddy simulations of Gloerfelt and Berland[30] the turbulent motions of the

boundary layer were initiated with a forward and subsequent backward facing step. Thus, the calculated distance from the leading edge in the predictions cannot be matched one-for-one with that in the LES simulations of Gloerfelt and Margnat.[31] Instead of directly matching $\mathcal{M}_\infty$ and $\mathcal{R}e_x$ we choose to match $\mathcal{M}_\infty$ and δ as reported by Gloerfelt and Margnat.[31] The size of the computational domain of the LES simulations is used to set the integration ranges of the acoustic source. In the presented predictions, we allow for the predicted variation of mean flow and turbulent statistics to change depending on x_l relative to the matched value of δ. By ensuring that these quantities match we have approximated the turbulent statistics of the LES simulations of Gloerfelt and Margnat[31] with the simplified mean flow model for the purposes of our task of validation. The equivalent conditions used to conduct predictions at the three conditions examined by Gloerfelt and Margnat[31] are summarized in Table 1. Observer positions are shown in Table 2. Note how close the observer is to the turbulent boundary layer. We estimate the extent of the equivalent computational domain in the streamwise direction as 9.1266×10^{-2} m and in the cross-stream direction as 3.8796×10^{-3} m. The ambient properties of the fluid are $c_\infty = 343.11$ m s^{-1}, $p_\infty = 101354.88$ Pa, $T_\infty = 293.0$ K, $\nu_\infty = 1.5098 \times 10^{-5}$ m^2 s^{-1}, and $\rho_\infty = 1.2053$ kg m^{-3}.

Figure 9 shows predictions of Eqn. 15 for sound pressure level (SPL) per unit Hz with respect to f in Hz at $\mathcal{M}_\infty = 0.50$, 0.70, and 0.90, where SPL $= 20 \log_{10}\left[S^{1/2}/(2 \times 10^{-5}\text{ Pa})\right]$. These three predictions are compared with the predictions of Gloerfelt and Margnat.[31] Simulations of Gloerfelt and Margnat[31] are shown as lines with symbols at $\mathcal{M}_\infty = 0.50$, 0.70, and 0.90 respectively, and predictions are a solid line for $\mathcal{M}_\infty = 0.50$, dashed line for $\mathcal{M}_\infty = 0.70$, and dashed-dotted line for $\mathcal{M}_\infty = 0.90$. Note symbols are used only to differentiate data and do not represent points of data. The constant $\mathcal{P}_f = 31622$, and it is set by matching the $\mathcal{M}_\infty = 0.50$ case. Predictions capture the same trends as measurement in that at low frequencies very little variation occurs in intensity. As the frequency increases the acoustic energy decreases rapidly. As $\mathcal{M}_\infty$ increases the SPL increases. It is noteworthy how energetic the acoustic waves are, but consider that the observers are only approximately 14δ from the wall and the boundary layer axial and spanwise extent are very large. The noise is very broadband, which is due to the large range of turbulent scales within the boundary layer. Overall, the predictions compare very well with the numerical results.

The scaling of Eqn. 15 with increasing velocity ($\mathcal{M}_\infty$ or u_∞) is shown in Fig. 10 as a solid line. The y-axis is the integrated auto-spectrum of acoustic pressure normalized to unity at $\mathcal{M}_\infty = 1$, and the x-axis is $\mathcal{M}_\infty$. Here, the Reynolds number of $\mathcal{R}e_x = 1 \times 10^6$ is held constant while u_∞ is varied. The observer is 10 m in the cross-stream direction from the center of a 1 m by 1 m flat plate. The same standard atmospheric properties are used as in the previous calculations. A dashed line is superimposed on the figure to illustrate the variation with u_∞^8. It is clear that the noise scales as u_∞^8. This is in agreement with the theoretical study of Powell[14] and the simulations of Gloerfelt and Margnat,[31] among others.

One advantage of the present approach is that far-field, mid-field, and near-field terms are separated within the integrand of the model equation. To demonstrate this advantage, we examine their intensities as a function of radiation distance at three frequencies. Figure 11 shows the SPL per unit f at 1, 10, and 100 kHz versus $y\delta^{-1}$. The noise from the far-field terms are solid lines, the noise from the mid-field terms are dashed lines, and the noise from the near-field terms are dashed-dotted lines. The flow is defined by $\mathcal{M}_\infty = 0.50$ and $\mathcal{R}e_x = 885500$, which results in $u_\tau = 7.70$, $y^+ = 1.96 \times 10^{-6}$, and $\delta = 1.195 \times 10^{-3}$ m. The observers are placed in the cross-stream direction starting at $\delta \approx 1.004$ from a point 68δ downstream from the leading edge. Ambient properties correspond to standard air. The extent of the domain in the axial and cross-stream directions is 9.127×10^{-2} m and 3.880×10^{-3} m, respectively. Note that the magnitudes of noise from the far-field terms are generally larger than from the mid-field, and the noise from the mid-field terms are generally higher than those of the near-field. We observe that the mid-field term is slightly more intense than the far-field term contribution only just outside the boundary layer at $y \approx \delta + \epsilon$. This is due to the observer distance being much smaller than unity and propagation distance powers of r^{-1} and r^{-2} for the far-field and mid-field terms, respectively. These trends are unlike those observed for the mid-field and near-field terms from jet mixing noise as discussed by Miller,[32] where very close to the jet the contributions from the mid-field and near-field terms dominate the overall intensity. As frequencies increase the intensities decrease. This is expected after examining the comparisons with predictions shown in Fig. 9. Recall that the far-field term decays as approximately r^{-1} and implies an approximately six dB reduction of SPL when the radiation distance is doubled. Within Figure 11 this is not observed because these predictions are in the near-field. Predictions conducted in the true far-field ($y >> \delta$) show a 6.0206 dB reduction, which is consistent with spherical spreading.

We now examine the spatial variation of coherence which is frequency dependent. Figure 12 shows the

coherence between two axially varying observers ($\boldsymbol{x} \neq \boldsymbol{x}'$) as a function of frequency. The coherence is calculated using Eqn. 16 and is shown as contours from zero to one. Here, the ambient Mach number is 0.30 and $\mathcal{R}e_x = 1 \times 10^6$. This corresponds to a flow with properties $\mathcal{R}e_\tau = 676.64$, $\mathcal{R}e_\theta = 1765.85$, $c_f = 3.963 \times 10^{-3}$, $u_\tau = 4.582$, y^+ one distance of 3.295×10^{-6} m, $\delta = 2.2295 \times 10^{-3}$ m, $\tau_w = 25.306$, and $\theta = 3.731 \times 10^{-4}$ m. The boundary layer is resolved using 10826 discrete points and the domain has a span of 10 m. Observer $\boldsymbol{x}$ is located at $x_l = 0.14668$ m from the leading edge of the flat plate, 4485δ in the cross-stream direction, and in the center of the wall. The second observer, $\boldsymbol{x}'$ is slowly varied from the initial location of $\boldsymbol{x}$ in the streamwise direction until approximately 1.1 x_l. The x-axis in Fig. 12 is normalized by x_l and the y-axis is $\mathcal{S}t$, which is dependent on u_∞ and δ. At low frequencies the spatial coherence is large, and as frequency increases the spatial coherence decreases. The acoustic radiation and its coherence is highly correlated with the turbulent field. Coefficients should be calibrated for the turbulent boundary layer, but unfortunately such data are not presently available. Nonetheless, the trends of coherence lengths are captured by the model.

Numerical Sensitivity Analysis

A sensitivity analysis is performed on the parameters involving l and α that are present within the length scale model and normalized two-point cross-correlation model. The numerical one-at-a-time sensitivity approach is selected for the $\mathcal{M}_\infty = 0.90$ case previously investigated. We vary the magnitude of each parameter by 1% and observe the relative change in power spectral density. The results of the numerical sensitivity analysis are shown in Fig. 13. The y-axis represents the change in SPL per unit f per 1% change in the associated arguments α, l_{sx}, l_{sy}, or l_{sz}. Here, α has almost no impact on the radiated noise. The streamwise length scale, which is larger relative to the cross-stream and spanwise length scale, is most sensitive, especially at high frequencies. The two minor length scales have much less effect on the radiated noise. Generally, the variation of radiated noise is less than 0.3 dB per 1% change per argument.

Summary, Conclusion, and Additional Effects

We have developed a closed-form mathematical model derived from the cross-spectral acoustic analogy for the auto-power and cross-power spectral densities of acoustic pressure radiating from a turbulent boundary layer. The arguments of the model depend on the mean flow and turbulent statistics of the boundary layer. These arguments could easily be calculated by numerical techniques but here have been approximated with a composite mean flow profile and simple analytic formula calibrated against measurement. This approach is adopted so that the capabilities of the model can be demonstrated and evaluation is quick. The developed arguments are compared with measurements to illustrate their variation with spatial position, Reynolds number, and Mach number. Models for the mean flow and turbulent statistics do not presently include the effect of pressure gradient, porosity, or wall roughness, but numerical simulation could easily capture these effects. Predictions of the auto-spectrum compare favorably with those derived from large eddy simulation. Predictions of spatial coherence, derived from the cross-spectrum, have similar characteristics to those observed from other flows and from the coherence of the turbulence within the boundary layer. The near-field, mid-field, and far-field intensity as a function of distance are investigated, and it was observed that only very near the boundary layer edge does the mid-field term have any contribution. Far from the boundary layer spherical spreading is recovered. An analysis of the prediction model shows that the power spectral density scales as the eighth power of velocity, which is expected from a turbulent source, and this is consistent with earlier theories. Hopefully in the future excellent experimental data will be available that measures the noise from boundary layer turbulence directly, that is not contaminated by other sources, so that this theory and its competitors can be directly compared with measurement. If this is accomplished, then the predicted spatial coherence of the acoustic field can also be directly compared with measurement. Like the studies for jet flows, it is expected that statistics of the acoustic field will be related to the statistics of the turbulent boundary layer.

Unfortunately, simple relations for the quantitative effects of pressure gradient, permeable walls, heated walls, or rough walls on the boundary layer mean flow, let alone turbulent statistics, are difficult to ascertain. Here, we briefly discuss current understanding and suggest that numerical simulation is currently the best method to capture these effects. Most industrial flows contain strong adverse or favorable pressure gradients in the axial direction within the turbulent boundary layer. In a review article by Kovasznay,[2] he characterizes

the pressure gradient using a non-dimensional approach with the non-dimensional pressure gradient, $K = -\nu(\rho u_\infty^3)^{-1}\partial p/\partial x$. Kline et al.[3] examined mean velocity profiles of various boundary layers characterized by K. Boundary layers with a mild pressure gradient are nearly in equilibrium, but for large K there is no equilibrium. Kline et al.[3] showed that the velocity profile possesses similarity in the outer region when normalized with shear velocity and possesses similarity within the inner region when normalized by u_τ. Thus, it is difficult to propose a composite profile like that shown previously that explicitly accounts for variation of K. Castillo,[58] who collapsed the mean flow for pipes and channel flows using power laws instead of log laws, showed that collapse of boundary layers in pressure gradients is possible. This latter approach opens the possibility of correctly predicting the mean flow with a pressure gradient but does not give any insight on its effect on the turbulence statistics.

Permeability or porosity of the wall has a significant effect on the turbulence and radiated noise. Unfortunately, the quantitative effect of wall permeability on turbulent statistics is not well understood. Manes et al.[19] attempted to alter the coefficients based on measurements in the logarithmic law region in the form $u^+ = \kappa^{-1}\log\left[(y+d)(z_0)^{-1}\right]$, where d is the zero plane position (depth of the porous material) and z_o is the aerodynamic roughness length. To characterize the effect of permeability, a porous Reynolds number, $\mathcal{R}e_{K_p} = K_p^{1/2}u_\tau\nu^{-1}$, was proposed where K_p is the porosity of the wall. Manes et al.[19] suggests that the coefficients in the log-law region are related to $\mathcal{R}e_{K_p}$ as $\kappa = 0.365\mathcal{R}e_{K_p}^{-0.19}$, $d^+ = 8.9\mathcal{R}e_{K_p}$, and $z_o^+ = 1.6\mathcal{R}e_{K_p} + \exp\left[-5K_p\right]$. In the context of Eqn. 20 we propose that the coefficients are related to Manes et al.[19] through the mappings: $\kappa \mapsto 0.365\mathcal{R}e_{K_p}^{-0.19}$ for $K_p > 0$, $y^+ \mapsto y^+ + d^+$, and $c_a \mapsto c_a z_0^{-1}$, assuming that the wall is weakly permeable.

Wall roughness can have significant impact on the intensity scaling of radiated acoustic waves. Wall roughness can be quantified by the characteristic roughness height, r_η, which is a nominal height of the material on the wall. Hersh[59] examined roughness within pipe flows and measured the noise radiated from an open end in the downstream direction. He showed that the effect of a rough wall is negligible in the frequency range of $\omega r_\eta u_\tau^{-1} < 5$. When roughness elements alter the statistics of turbulence of the boundary layer and r_η is large then additional noise from roughness elements must be accounted for. Noise from roughness elements that do not significantly alter turbulent statistics can be predicted with the approach of Howe.[26] When the turbulent statistics are altered by significant wall roughness, then the mean flow and turbulent statistics models must be dependent on r_η.

Acknowledgments

The photograph of the turbulent boundary layer in Fig. 1 was kindly provided by Jung Lee and colleagues (Lee et al.[4]) and used with permission. The author is grateful for four excellent anonymous reviews and comments of the associate editor, which resulted in a greatly improved article.

References

[1]Prandtl, L., "On Fluid Motion with Very Small Friction," *Heidelberg Mathematical Congress*, 1904.

[2]Kovasznay, L. S. G., "The Turbulent Boundary Layer," *Annual Review of Fluid Mech.*, Vol. 2, No. 1, 1970, pp. 95–112. doi:10.1146/annurev.fl.02.010170.000523.

[3]Kline, S. J., Reynolds, W. C., Schraub, F. A., and Runstadler, P. W., "The Structure of Turbulent Boundary Layers," *Journal of Fluid Mechanics*, Vol. 30, No. 4, 1967, pp. 741–773. doi:10.1017/s0022112067001740.

[4]Lee, J. H., Kwon, Y. S., Monty, J. P., and Hutchins, N., "Tow-Tank Investigation of the Developing Zero-Pressure-Gradient Turbulent Boundary Layer," *18th Australasian Fluid Mechanics Conference*, 2012.

[5]Eichelbrenner, E. A., "Three-Dimensional Boundary Layers," *Annual Review of Fluid Mech.*, Vol. 5, No. 1, 1973, pp. 339–360. doi:10.1146/annurev.fl.05.010173.002011.

[6]Schlichting, H. and Gersten, K., "Boundary-Layer Theory," *Springer*, 2000.

[7]Hunt, J. C. R., Moin, P., Moser, R. D., and Spalart, P. R., "Self Similarity of Two Point Correlations in Wall Bounded Turbulent Flows," *Center for Turbulence Research, Proceedings of the Summer Program*, 1987.

[8]Hunt, J. C. R., Moin, P., Lee, M., Moser, R. D., Spalart, P., Mansour, N. N., Kaimal, J. C., and Gaynor, E., "Cross Correlation and Length Scales in Turbulent Flows Near Surfaces," *NASA TM-111344*, 1989.

[9]Naka, Y., Stanislas, M., Foucaut, J. M., Coudert, S., Laval, J. P., and Obi, S., "Space-Time Pressure-Velocity Correlations in a Turbulent Boundary Layer," *Journal of Fluid Mechanics*, Vol. 771, 2015, pp. 624–675. doi:10.1017/jfm.2015.158.

[10]Robinson, S. K., "Coherent Motions in the Turbulent Boundary Layer," *Annual Review of Fluid Mech.*, Vol. 23, No. 1, 1991, pp. 601–639. doi:10.1146/annurev.fl.23.010191.003125.

[11]Robinson, S. K., "Space-Time Correlation Measurements in a Compressible Turbulent Boundary Layer," *4th Joint Fluid Mechanics, Plasma Dynamics and Lasers Conference, AIAA Paper 1986-1130*, 1986. doi:10.2514/6.1986-1130.

[12]Spina, E. F. and Smits, A. J., "Organized Structures in a Compressible, Turbulent Boundary Layer," *Journal of Fluid Mechanics*, Vol. 182, 1987, pp. 85–109. doi:10.1017/s0022112087002258.

[13]Morkovin, M., "Effects of Compressibility on Turbulent Flows," *International Symposium on the Mechanics of Turbulence*, 1962, pp. 367–380.

[14]Powell, A., "Aerodynamic Noise and the Plane Boundary," *Journal of the Acoustical Society of America*, Vol. 32, No. 8, 1960, pp. 982–990. doi:10.1121/1.1908347.

[15]Rackl, R. and Weston, A., "Modeling of Turbulent Boundary Layer Surface Pressure Fluctuation Auto and Cross Spectra - Verification and Adjustments Based on TU-144LL Data," *NASA CR 2005-213939*, 2005.

[16]Efimtsov, B. M., "Characteristics of the Field of Turbulent Wall Pressure Fluctuations at Large Reynolds Numbers," *Soviet Physics Acoustics*, Vol. 28, No. 4, 1982, pp. 289–292.

[17]Palumbo, D., "Determining Correlation and Coherence Lengths in Turbulent Boundary Layer Flight Data," *Journal of Sound and Vibration*, Vol. 331, No. 16, 2012, pp. 3721–3737. doi:10.1016/j.jsv.2012.03.015.

[18]Alexander, W., Devenport, W., Glegg, S., and Van Buren, R., "Directivity of Noise from Discrete Elements in a Turbulent Boundary Layer," *16th AIAA/CEAS Aeroacoustics Conference, AIAA Paper 2010-3773*, 2010. doi:10.2514/6.2010-3773.

[19]Manes, C., Poggi, D., and Ridolfi, L., "Turbulent Boundary Layers Over Permeable Walls: Scaling and Near-Wall Structure," *Journal of Fluid Mechanics*, Vol. 687, 2011, pp. 141–170. doi:10.1017/jfm.2011.329.

[20]Greshilov, E. M. and Mironov, M. A., "Experimental Evaluation of Sound Generated by Turbulent Flow in a Hydrodynamic Duct," *Soviet Physics - Acoustics*, Vol. 29, No. 4, 1983, pp. 275–280.

[21]Duell, E., Walter, J., Arnette, S., and Yen, J., "Boundary Layer Noise in Aeroacoustic Wind Tunnels," *42nd AIAA Aerospace Sciences Meeting and Exhibit, AIAA Paper 2004-1028*, 2004. doi:10.2514/6.2004-1028.

[22]Smith, B., Alexander, W., Devenport, W., Glegg, S., and Grissom, D., "The Relationship Between Roughness Noise and the Near-Field Pressure Spectrum," *AIAA Aeroacoustics Conference, AIAA Paper 2008-2904*, 2008. doi:10.2514/6.2008-2904.

[23]Ffowcs Williams, J. E., "Sound Radiation from Turbulent Boundary Layers Formed on Compliant Surfaces," *Journal of Fluid Mechanics*, Vol. 22, No. 2, 1965, pp. 347–358. doi:10.1017/s0022112065000794.

[24]Ffowcs Williams, J. E., "The Acoustics of Turbulence Near Sound-Absorbent Liners," *Journal of Fluid Mechanics*, Vol. 51, No. 4, 1972, pp. 737–749. doi:10.1017/s0022112072001338.

[25]Ffowcs Williams, J. E. and Purshouse, M., "A Vortex Sheet Modelling of Boundary-Layer Noise," *Journal of Fluid Mechanics*, Vol. 113, 1981, pp. 187–220. doi:10.1017/s0022112081003455.

[26]Howe, M. S., "Surface Pressures and Sound Produced by Turbulent Flow Over Smooth and Rough Walls," *Journal of the Acoustical Society of America*, Vol. 90, No. 2, 1991, pp. 1041–1047. doi:10.1121/1.402292.

[27]Glegg, S., Devenport, W., Grissom, D., and Smith, B., "Rough Wall Boundary Layer Noise: Theoretical Predictions," *13th AIAA/CEAS Aeroacoustics Conference (28th AIAA Aeroacoustics Conference), AIAA Paper 2007-3417*, 2004. doi:10.2514/6.2007-3417.

[28]Hu, Z., Morfey, C., and Sandham, N. D., "Sound Radiation in Turbulent Channel Flows," *Journal of Fluid Mechanics*, Vol. 475, 2003. doi:10.1017/s002211200200277x.

[29]Hu, Z., Morfey, C., and Sandham, N. D., "Sound Radiation from a Turbulent Boundary Layer," *Physics of Fluids*, Vol. 18, No. 9, 2006, pp. 1–4. doi:10.1063/1.2337733.

[30]Gloerfelt, X. and Berland, G., "Turbulent Boundary-Layer Noise: Direct Radiation at Mach Number 0.5," *Journal of Fluid Mechanics*, Vol. 723, 2013, pp. 318–351. doi:10.1017/jfm.2013.134.

[31]Gloerfelt, X. and Margnat, F., "Effect of Mach number on Boundary Layer Noise," *20th AIAA/CEAS Aeroacoustics Conference, AIAA Paper 2014-3291*, 2014. doi:10.2514/6.2014-3291.

[32]Miller, S. A. E., "Prediction of Near-Field Jet Cross Spectra," *AIAA Journal*, Vol. 53, No. 8, 2015, pp. 2130–2150. doi:10.2514/1.J053614.

[33]Miller, S. A. E., "On Theoretical Broadband Shock-Associated Noise Near-Field Cross-Spectra," *AIAA Aviation and Aeronautics Forum and Exposition (21st AIAA/CEAS Aeroacoustics Conference), AIAA Paper 2015-2832*, 2015. doi:10.2514/6.2015-2832.

[34]Lighthill, M. J., "On Sound Generated Aerodynamically. I. General Theory," *Proc. R. Soc. Lond. A.*, Vol. 211, No. 1107, 1952, pp. 564–587. doi:10.1098/rspa.1952.0060.

[35]Lighthill, M. J., "On Sound Generated Aerodynamically. II. Turbulence as a Source of Sound," *Proc. R. Soc. Lond. A.*, Vol. 222, No. 1148, 1954, pp. 1–32. doi:10.1098/rspa.1954.0049.

[36]Hanson, D. B. and Magliozzi, B., "Propagation of Propeller Tone Noise Through a Fuselage Boundary Layer," *Journal of Aircraft*, Vol. 22, No. 1, 1985, pp. 63–70. doi:10.2514/3.45081.

[37]Mcaninch, G. and Rawls, J. R., "Effects of Boundary Layer Refraction and Fuselage Scattering on Fuselage Surface Noise from Advanced Turboprop Propellers," *22nd Aerospace Sciences Meeting*, 1984. doi:10.2514/6.1984-249.

[38]Lu, H., "Fuselage Boundary Layer Effects on Sound Propagation and Scattering," *12th AIAA Aeroacoustics Conference*, 1989. doi:10.2514/6.1989-1098.

[39]Smith, M. G. and Morfey, C. L., "Directivity and Sound Power Radiated by a Source Under a Boundary Layer," *AIAA Journal*, Vol. 44, No. 11, 2006, pp. 2630–2635. doi:10.2514/1.19138.

[40]Suzuki, T. and Lele, S. K., "Green's Functions for a Source in a Boundary Layer: Direct Waves, Channelled Waves and Diffracted Waves," *Journal of Fluid Mechanics*, Vol. 477, 2003, pp. 129–173. doi:10.1017/S0022112002003099.

[41]Lilley, G. M., "On the Noise from Jets," *AGARD Conference Proceedings In Noise Mechanisms*, Vol. 13, 1974, pp. 1–11.

[42]Goldstein, M. E., "A Generalized Acoustic Analogy," *Journal of Fluid Mechanics*, Vol. 488, 2003, pp. 315–333. doi:10.1017/S0022112003004890.

[43]Lighthill, M. J., "Aerodynamic Noise, or, Turbulence as a Source of Sound," *Fluid Motion Sub-Committee Aeronautical Research Council*, 1950, pp. 1–26.

[44]Ribner, H., "Theory of Two-Point Correlations of Jet Noise," *NASA TN D-8330*, 1976.

[45]Ffowcs Williams, J. E., "The Noise from Turbulence Convected at High Speed," *Phil. Trans. R. Soc. Lond. A*, Vol. 255, No. 1063, 1963, pp. 469–503. doi:10.1098/rsta.1963.0010.

[46]Palumbo, D., "The Variance of Convection Velocity in the Turbulent Boundary Layer and its Effect on Coherence Length," *Journal of Sound and Vibration*, Vol. 332, No. 15, 2013, pp. 3692–3705. doi:10.1016/j.jsv.2013.02.010.

[47]Zwillinger, D., "Table of Integrals, Series, and Products," *Academic Press*, 2015.

[48]Degani, A. T., Smith, F. T., and Walker, J. D. A., "The Structure of a Three-Dimensional Turbulent Boundary Layer," *Journal of Fluid Mechanics*, Vol. 250, 1993, pp. 43–68. doi:10.1017/s0022112093001375.

[49]Musker, A. J., "Explicit Expression for the Smooth Wall Velocity Distribution in a Turbulent Boundary Layer," *AIAA Journal*, Vol. 17, No. 6, 1979, pp. 655–657. doi:10.2514/3.61193.

[50]Coles, D., "The Law of the Wake in the Turbulent Boundary Layer," *Journal of Fluid Mechanics*, Vol. 1, No. 2, 1956, pp. 191–226. doi:10.1017/s0022112056000135.

[51]Huang, P. G. and Coleman, G. N., "Van Driest Transformation And Compressible Wall-Bounded Flows," *AIAA Journal*, Vol. 32, No. 10, 1994, pp. 2110–2113. doi:10.2514/3.12259.

[52]Walz, A., "The Noise from Turbulence Convected at High Speed," *The MIT Press*, 1969.

[53]Jimenez, J., Hoyas, S., Simens, M. P., and Mizuno, Y., "Turbulent Boundary Layers and Channels at Moderate Reynolds Numbers," *Journal of Fluid Mechanics*, Vol. 657, 2010, pp. 335–360. doi:10.1017/S0022112010001370.

[54]Erm, L. P. and Joubert, P. N., "Low-Reynolds-Number Turbulent Boundary Layers," *Journal of Fluid Mechanics*, Vol. 230, 1991, pp. 1–44. doi:10.1017/s0022112091000691.

[55]Duan, L., Beekman, I., and Martin, M. P., "Direct Numerical Simulation of Hypersonic Turbulent Boundary Layers. Part 3. Effect of Mach number," *Journal of Fluid Mechanics*, Vol. 672, 2011, pp. 245–267. doi:10.1017/s0022112010005902.

[56]Gloerfelt, X., "The Link Between Wall Pressure Spectra and Radiated Sound from Turbulent Boundary Layers," *16th AIAA/CEAS Aeroacoustics Conference, AIAA Paper 2010-3904*, 2010. doi:10.2514/6.2010-3904.

[57]Cohen, E. and Gloerfelt, X., "Effect of Pressure Gradients on Turbulent Boundary Layer Noise and Wall-Pressure Fluctuations," *21st AIAA/CEAS Aeroacoustics Conference, AIAA Paper 2015-3117*, 2015. doi:10.2514/6.2015-3117.

[58]Castillo, L., "Similarity Analysis of Turbulent Boundary Layers," *State University of New York at Buffalo, Ph.D. Dissertation*, 1977.

[59]Hersh, A., "Experimental Investigation Of Surface Roughness Generated Flow Noise," *8th AIAA Aeroacoustics Conference, AIAA Paper 1983-768*, 1983. doi:10.2514/6.1983-786.

Tables

Table 1. Properties of the turbulent boundary layer for comparisons of the prediction model with numerical simulation.

$\mathcal{M}_\infty$	$\mathcal{R}e_x$	u_∞ ms^{-1}	δ m	c_f	u_τ	x_l m	τ_w	$y+$	$\mathcal{R}e_\theta$	k_{max} m^{2}s^{-2}
0.50	885500	171.6	1.195×10^{-3}	4.034×10^{-3}	7.705	0.0780	071.5	1.960×10^{-6}	1511	252
0.70	773000	240.2	7.526×10^{-4}	4.115×10^{-3}	10.90	0.0486	143.1	1.386×10^{-6}	1322	465
0.90	820000	308.8	6.183×10^{-4}	4.080×10^{-3}	13.95	0.0401	234.4	1.083×10^{-6}	1396	765

Table 2. Locations of the acoustic observer for comparisons of prediction model with numerical simulation. Here, subscripts of x denote the vector component.

$\mathcal{M}_\infty$	x_1 m	x_2 m	x_3 m	$x_1\delta^{-1}$	$x_2\delta^{-1}$	$x_3\delta^{-1}$
0.50	8.126×10^{-2}	1.63715×10^{-2}	0	68.00	13.70	0
0.70	5.798×10^{-2}	1.16715×10^{-2}	0	77.04	15.51	0
0.90	4.511×10^{-2}	9.08460×10^{-3}	0	72.97	14.70	0

Figures

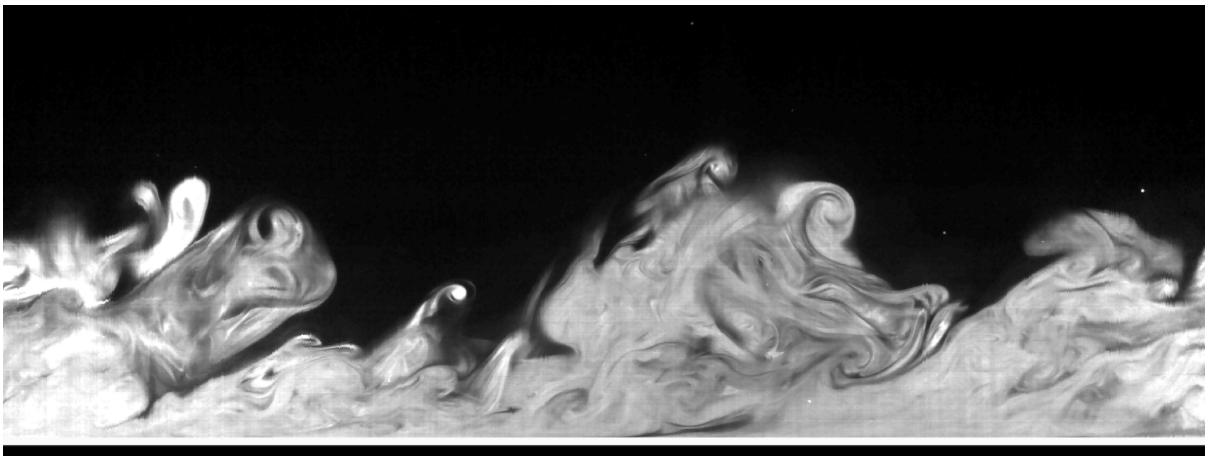

Figure 1. Photograph of a high Reynolds number turbulent boundary layer, moving from left to right, which is illuminated by laser induced fluorescence. The photograph is courtesy of Lee et al.[4]

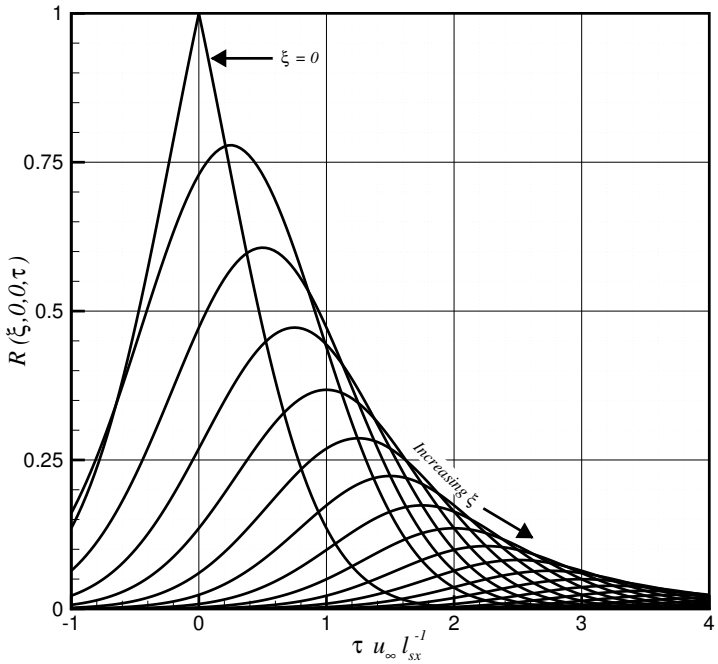

Figure 2. Normalized two-point cross-correlation within the turbulent boundary layer at various separation distances ξ.

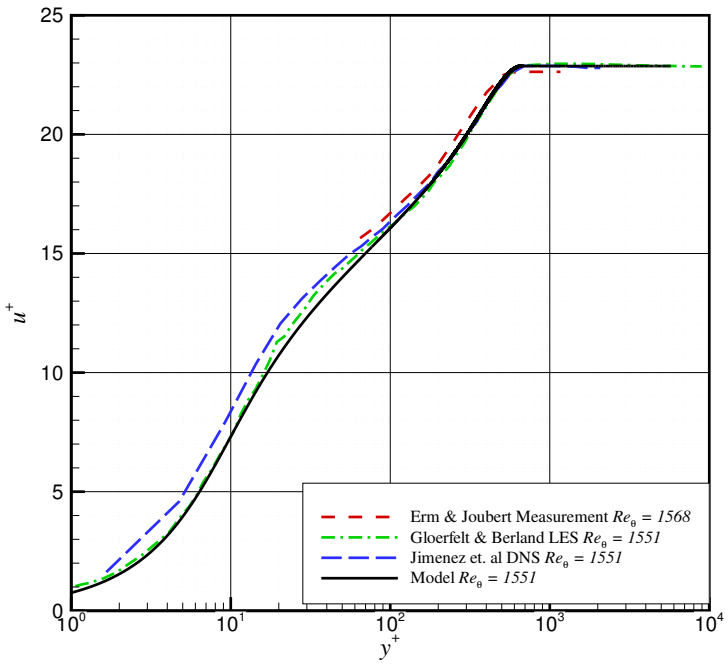

Figure 3. Comparison of the model for streamwise velocity profile with numerical simulation and experiment.

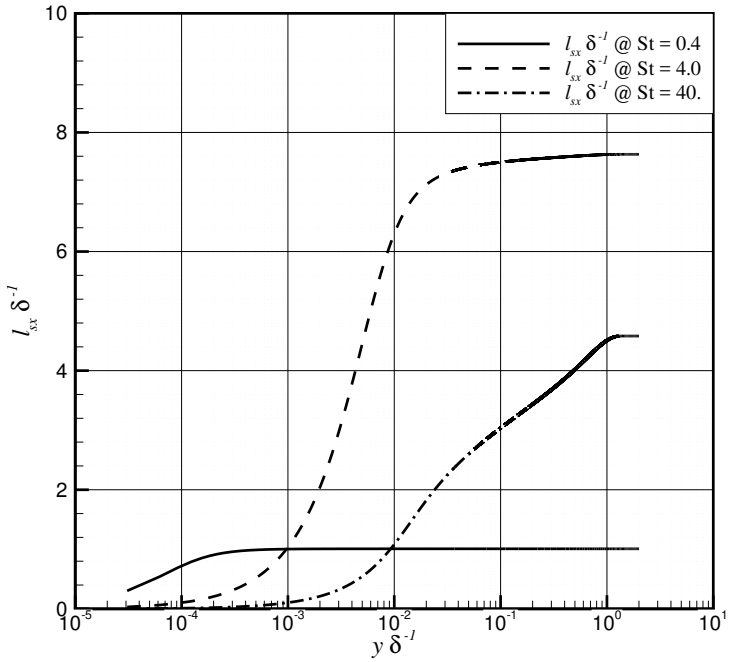

Figure 4. Variation of the streamwise length scale with cross-stream position at three Strouhal numbers.

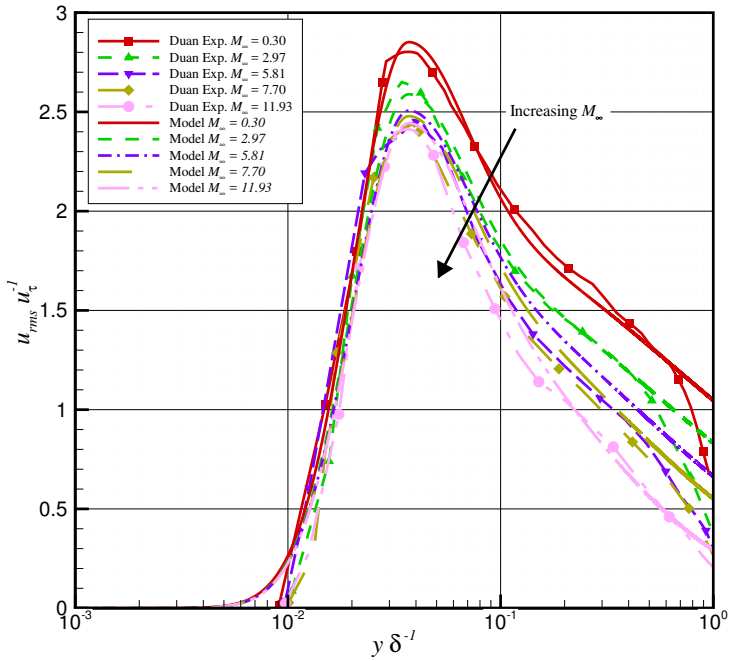

Figure 5. Comparisons of the model for $(\overline{u'u'})^{1/2}$ with the measurements of Duan et al.[55] for a wide range of $\mathcal{M}_\infty$ within the boundary layer.

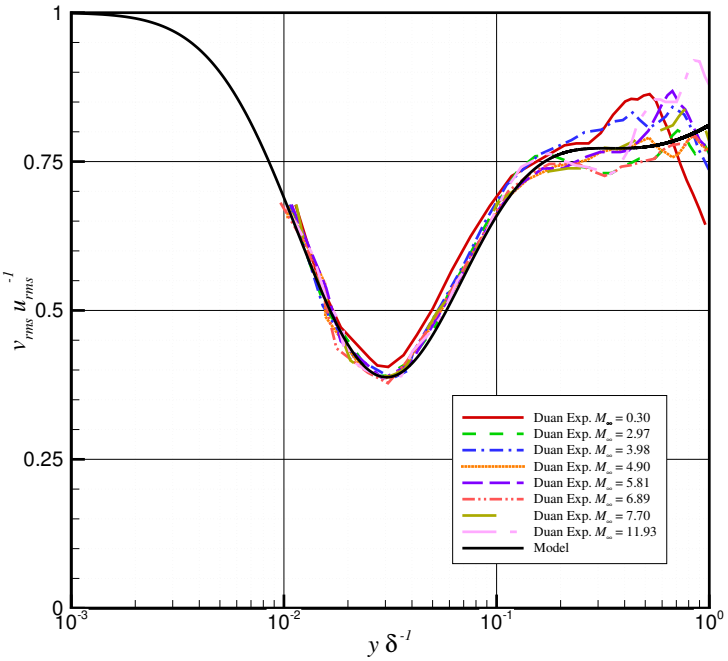

Figure 6. Comparisons of the model for $(\overline{v'v'})^{1/2}(\overline{u'u'})^{-1/2}$ with the measurements of Duan et al.[55] for a wide range of $\mathcal{M}_\infty$ within the boundary layer.

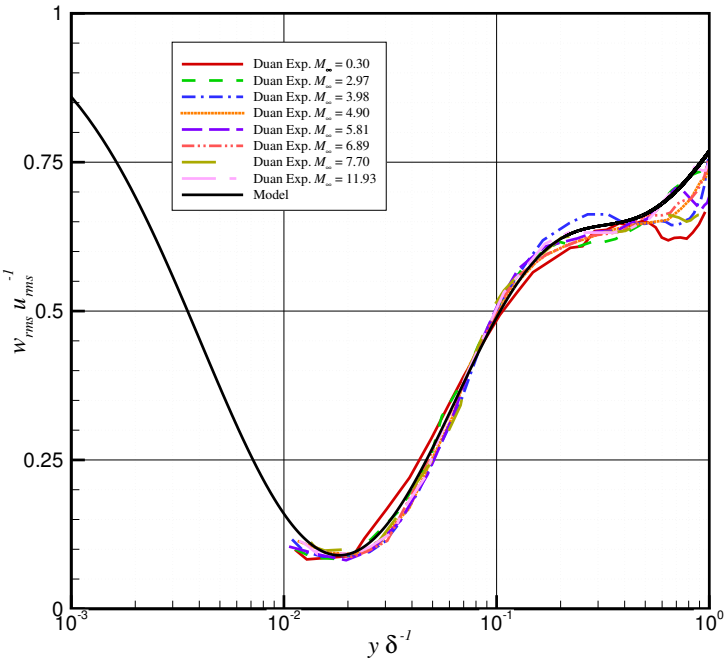

Figure 7. Comparisons of the model for $(\overline{w'w'})^{1/2}(\overline{u'u'})^{-1/2}$ with the measurements of Duan et al.[55] for a wide range of $\mathcal{M}_\infty$ within the boundary layer.

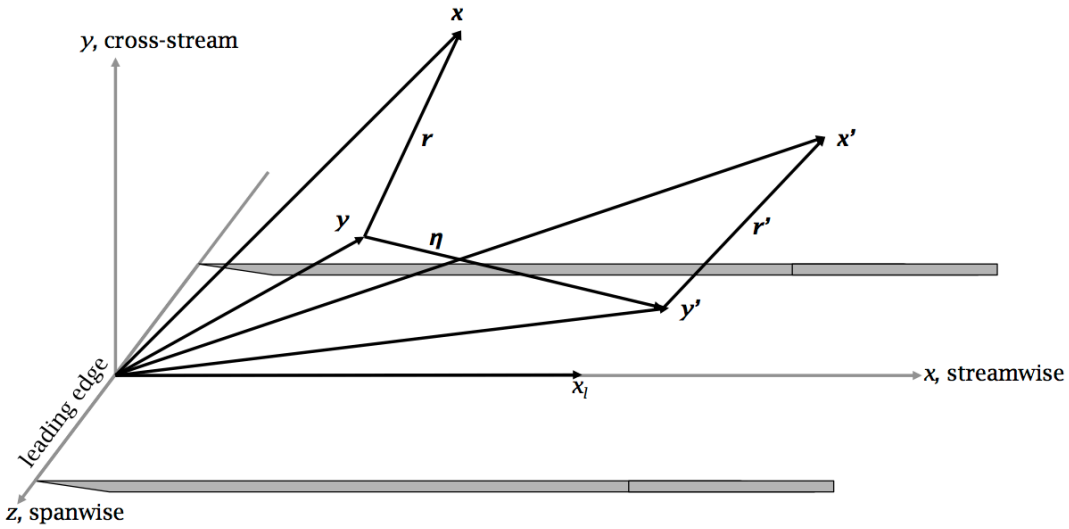

(a) Both source positions are within the boundary layer.

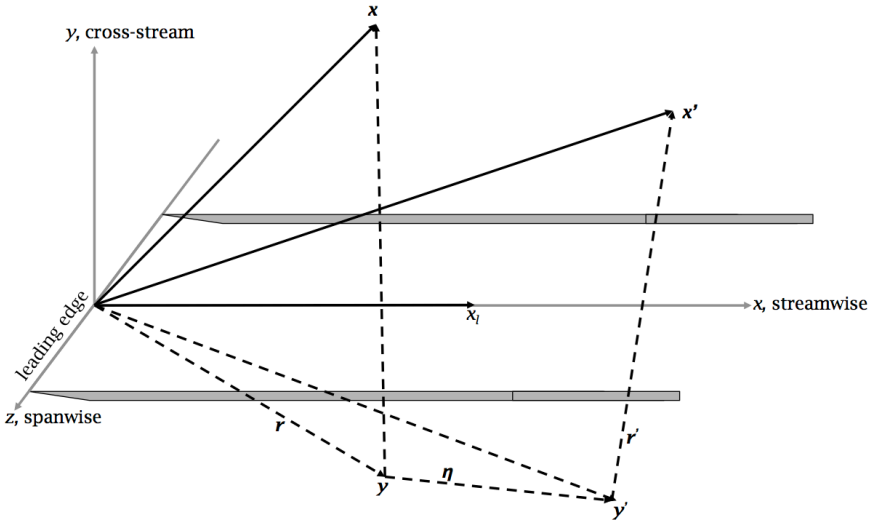

(b) Both source positions are within the mirrored boundary layer.

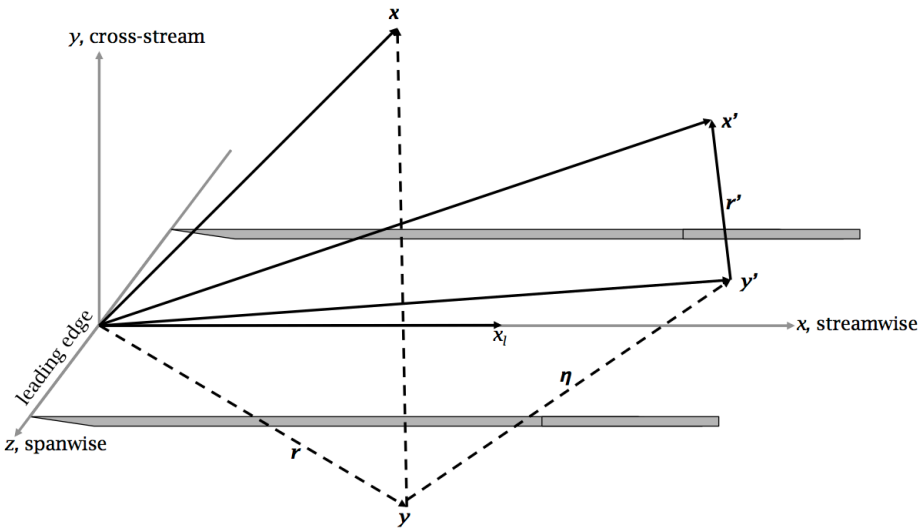

(c) One source position within the boundary layer and the second within the mirror.

Figure 8. Coordinate system.

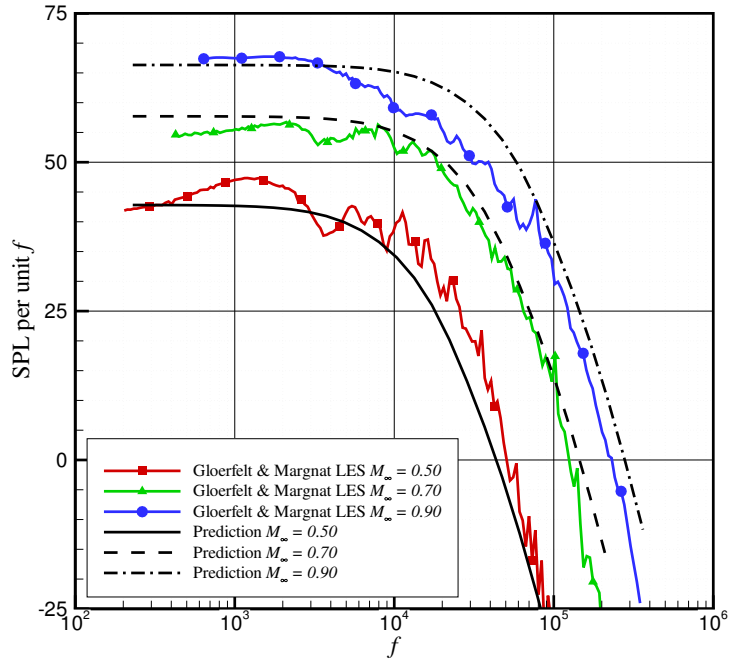

Figure 9. Predictions of sound pressure level per unit Hz compared with the numerical simulations of Gloerfelt and Margnat[31] at three different conditions.

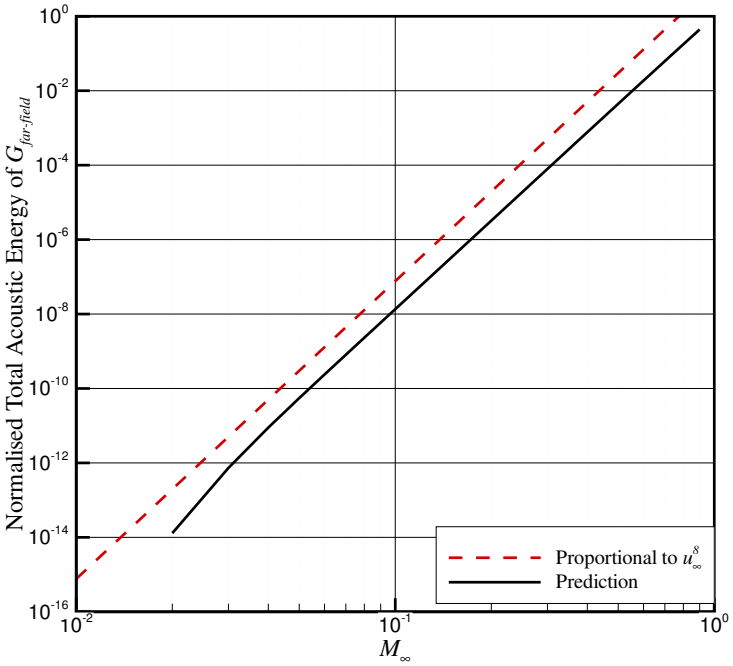

Figure 10. Predictions of total acoustic energy with varying $\mathcal{M}_\infty$.

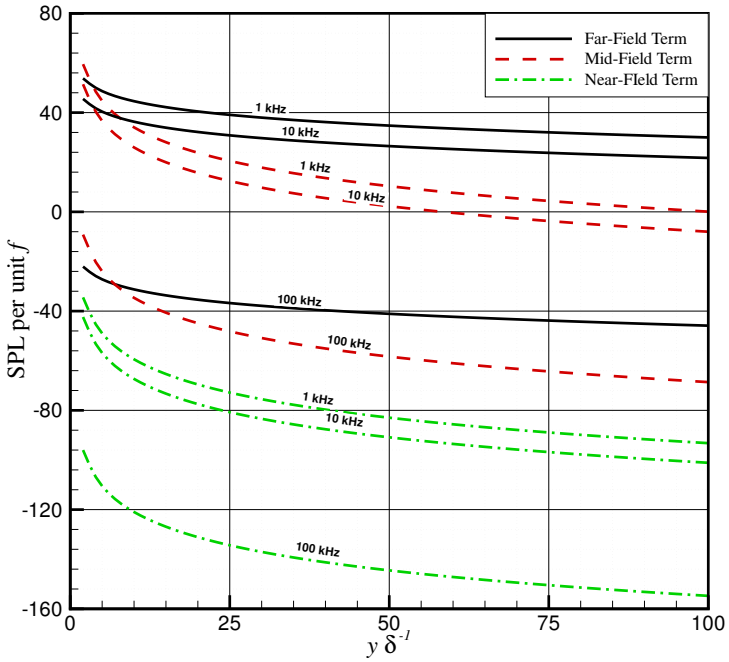

Figure 11. Sound pressure level per unit f at multiple frequencies of the far-field, mid-field, and near-field terms decaying with increasing $y\delta^{-1}$.

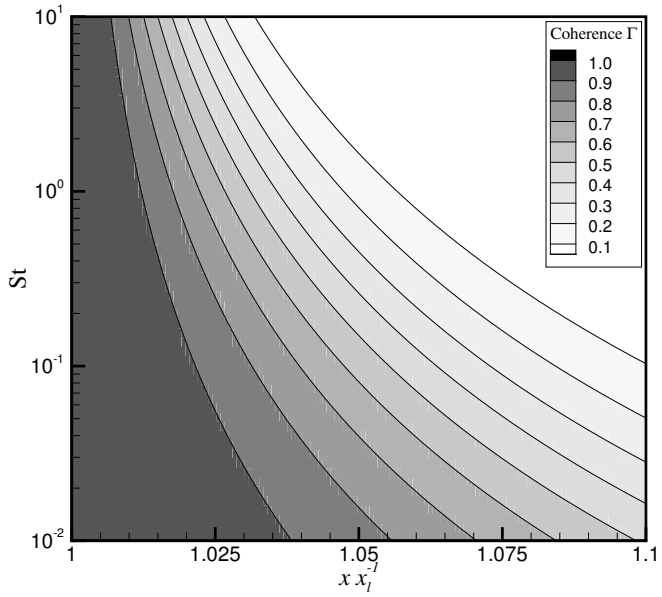

Figure 12. Spatially varying coherence of the acoustic pressure as a function of St.

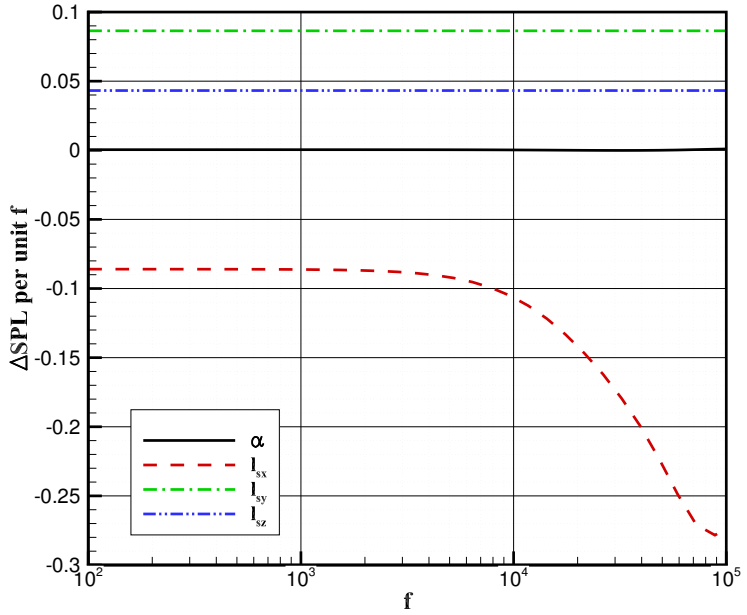

Figure 13. Sensitivity analysis of source correlation arguments α, l_{sx}, l_{sy}, and l_{sz}.